Shade and Light Modeling for Agrivoltaic Systems

with Focus on Single-Axis Agrivoltaic Systems

Mahta Keivani Najafabadi

Master's thesis
2024:E14

Lund University

Faculty of Science
Centre for Mathematical Sciences
Mathematical Statistics

Centrum Scientiarum Mathematicarum

Shade and Light Modeling for Agrivoltaic Systems

With Focus on Single-Axis Agrivoltaic Systems

by Mahta Keivani Najafabadi

LUND
UNIVERSITY

Master's Thesis

Supervisor: Johan Lindström
Examiner: Linda Hartman

2024

Abstract

Global population growth presents challenges to sustainable food and energy production. Transitioning to renewable energy sources, like solar power, requires significant land allocations, conflicting with the need for arable farmland. Agrivoltaics (AV) offers a potential solution by integrating crops and solar panels on the same land. Ensuring consistent and adequate agricultural output alongside energy production becomes crucial with AV system implementation. Therefore, it is important to evaluate the effects of shading from photovoltaic (PV) systems on crop yield and to optimize the design of AV systems for maximum agricultural productivity and energy generation. This project aims to develop a model for simulation of the shade on the ground caused by the photovoltaic structure on the field, focusing on PV systems with single-axis tracking. The model enables the evaluation of the distribution of photosynthetically active radiation (PAR) at crop level, essential for crop growth. Given the lack of PAR measurements for many potential agriPV sites, we employ simple regression models to estimate PAR from readily available solar radiation data. The total solar radiation is divided into its diffuse and direct components, with a shading factor methodology used to determine the amount of each type of radiation reaching the ground in the AV system. These shading factors represent the proportion of reduction in each radiation component. This process involves using a three-dimensional model to simulate, at each time step, the precise shape and area of the shadows cast on the ground by the PV system. The model accurately simulates shading between rows of PV panels in AV systems, allowing computation of received light considering shading effects. By dividing the area into a grid and calculating shading factors for each cell separately, we assess shade and light distribution on the ground. Extending the model designed for single-axis tracker AV systems, our methodology can assess shading effects in systems with fixed tilt or two-axis trackers, underscoring its adaptability across different AV system types. Preliminary results from the model indicate that the amount of light and shading received at crop level

in AV systems, depend on both system design and geographic location. Additionally, the analysis of shading distribution between rows of solar panels reveals how crops experience varying degrees of radiation reduction in different areas between the panels. Furthermore, for more accurate estimation of available PAR, employing models adjusted to local weather conditions is preferable.

Popular science summary

Combining agricultural practices with solar power production presents a promising solution to our increasing energy demands while also ensuring food security. This innovative strategy, known as agrivoltaics (AV), responds to the growing global population's demand for more sustainable food and energy production practices. In our project, we aimed to develop a simulation model to simulate shading caused by solar panels on the ground to help us understand how shading impacts crop growth in AV settings. By accurately determining how much light, at different times, reaches the ground in AV systems, we can optimize AV system design for maximum energy and agricultural productivity. Our focus was on systems where solar panels track the sun's movements along a single axis of rotation. However, the model is adaptable to various AV setups, including those with fixed-angle solar panels or panels that rotate around two axes. Additionally, we estimated the photosynthetically active radiation (PAR), crucial for crop growth, from solar radiation data and used it to calculate the crop-relevant light received on the ground in an AV system. Our initial findings suggest that the amount of light and shading experienced by crops depends on system design and location. Moreover, analyzing shading distribution between solar panel rows reveals variations in radiation reduction across crop areas. For more precise estimation PAR, employing models tailored to local weather conditions proved advantageous. This project contributes to optimizing AV systems for enhanced agricultural productivity and energy generation while addressing global sustainability challenges.

Acknowledgements

I extend my heartfelt thanks to my supervisor, Johan Lindström, for his invaluable guidance and support throughout this thesis. His expertise and constructive feedback have been instrumental in shaping my research journey.

I also express my sincere gratitude to OX2 for their invaluable collaboration and support throughout this project.

Contents

List of Abbreviations

Abbreviation	Description	Unit	Page
BHI	Direct (Beam) Horizontal Irradiance	W/m^2	8
DHI	Diffuse Horizontal Irradiance	W/m^2	8
GHI	Global Horizontal Irradiance	W/m^2	8
GHI_s	Shaded Global Horizontal Irradiance	W/m^2	9
LHI	Light Homogeneity Index	(%) Percent	34
PAR	Photosynthetically Active Radiation	W/m^2	8
PAR_b	Direct Photosynthetically Active Radiation	W/m^2	8
PAR_d	Diffuse Photosynthetically Active Radiation	W/m^2	8
PAR_s	Shaded Photosynthetically Active Radiation	W/m^2	9
PPFD	Photosynthetic Photon Flux Density	$\mu mol/m^2/s$	8

Chapter 1

Introduction

1.1 Background

As the global population rises, many countries are facing significant hurdles in producing sustainable food and energy. Transitioning from fossil fuels to renewable energy sources, like solar farms, demands vast land areas, sometimes at odds with the need for cultivable terrain [1]. Especially since flatlands that are ideal for agriculture, are equally favorable for building solar farms [25]. A potential solution is agrivoltaics (AV), a practice introduced in 1982 [16] , where crops and solar panels coexist on the same plot of land. Given the competing land demands of food and energy production, it is vitally important to ensure consistent and sufficient agricultural output when employing AV systems [48].

Many field studies have been carried out to assess the impact of shading from photovoltaic (PV) system on the yield of different crops [29, 43, 47, 48]. While these studies highlight varying effects on different crops due to the shading and reduced radiation caused by the presence of PV systems, accurately modeling the shading effects of rows of PV panels at crop level remains crucial. It is possible to minimize the reduction in crop yield by using shade-tolerant crops [10]. Understanding the shading and change in the amount of radiation on the crops in AV systems can be used to adapt the design of the PV system to the need of specific crops [2].

1.2 Aim

The aim of this project is to develop a model for simulation of the shade on the ground caused by the presence of photovoltaic structure on the field. This result can then be used to evaluate the distribution of the crop relevant light, also known as photosynthetically active radiation (PAR), on the ground. Since PAR measurements are not available for all potential agrivoltaic sites, simple models are to be employed for estimation of PAR from solar radiation data that is easily accessible for most locations on earth.

Chapter 2

Theoretical Framework

2.1 Overview

This chapter starts by introducing key concepts related to solar energy and radiation, essential for understanding this work, in Section 2.2. Next in Section 2.3, we present an overview of the most commonly used methods and techniques for modeling shade, particularly in the context of agrivoltaics. Finally, Section 2.4 explores different strategies for estimating and modeling photosynthetically active radiation (PAR), which is essential for crop growth.

2.2 Solar radiation

Our aim in this section is not to dive into the details of solar energy but to introduce some basic concepts and relations that are essential for understanding light and shade modeling within the context of agrivoltaics.

Energy is emitted from the sun and disperses throughout space as electromagnetic radiation in various directions [5]. Electromagnetic radiation is commonly categorized into distinct wavelength groups. The solar radiation that reaches the top of Earth's atmosphere covers wavelengths from approximately 0.2 μm to 4.0 μm including the photosynthetically active radiation (PAR) [5]. This range of wavelengths

are crucial to Earth and its atmosphere and are of critical importance in supporting life on Earth.

Irradiance is a measure of the radiant flux received per unit area of surface. It quantifies the rate at which electromagnetic energy is incident on a surface, typically expressed in watts per square meter W/m^2. This concept is distinct from radiant flux, which denotes the total amount of radiant energy emitted, absorbed by a surface per unit time, expressed in joules per second, or watts ($J/s = W$), and from radiant energy, which includes the complete electromagnetic energy radiated in all directions measured in joules (J) [24].

To model solar radiation, several key concepts need to be introduced. In Section 2.2.1, we discuss the solar angles that determine the sun's position. Next, Section 2.2.2 introduces the concept of extraterrestrial solar radiation. Lastly, Section 2.2.3 presents various measures of solar radiation at the Earth's surface.

2.2.1 Solar angles

Due to the vast distance between the Earth and the sun, the sun appears as a sphere with a small apparent diameter. For this reason, the sun's rays are essentially parallel at the top of the atmosphere [46]. The location of the sun can be defined by two angles: the solar zenith angle and solar azimuth angle. The solar zenith angle is the angle between the sun's rays and the local vertical, while the solar azimuth angle, increasing clockwise, is the angle between the sun's rays projected on the horizontal plane and the vector pointing to north [46].The solar azimuth angle varies from 0 to 2π. The solar zenith angle, which ranges from zero to $\pi/2$, is zero when the sun is directly overhead and increases as the sun descends towards the horizon, reaching its maximum value of $\pi/2$ at both sunrise and sunset [46]. The solar elevation angle is defined as the angle between sun's rays and the horizontal plane and is the complement to the solar zenith angle [46]. It consequently ranges from 0 to $\pi/2$, reaching its minimum when the sun is on the horizon during sunrise and sunset and its maximum value when the sun is at its peak in the sky [46]. Figure 2.1 illustrates the solar angles. The solar rays' direction at the top of the atmosphere is almost identical to that seen by an observer on Earth, with atmospheric refraction causing only minor variation, as a result, solar angles are virtually the same at any altitude, whether observed from the ground or the top of the atmosphere [46].

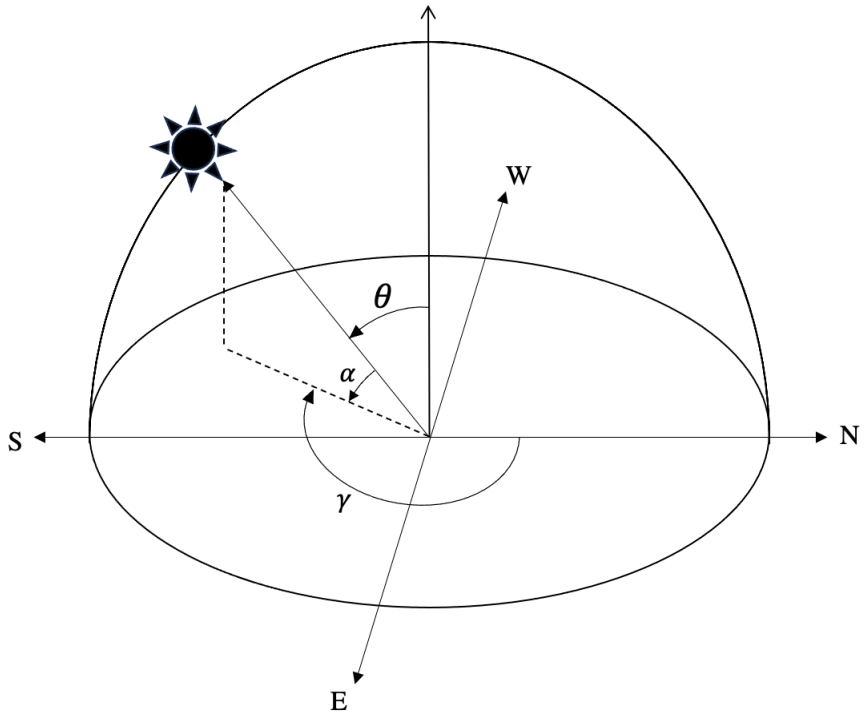

Figure 2.1: Positon of the sun is defined by solar azimuth angle γ measured clockwise from north and the solar zenith angle θ which is the complementary of the solar elevation angle α

2.2.2 Extraterrestrial solar radiation

The amount of the solar radiation received on a surface normal to the sun's rays, in watts per unit area, at the top of the atmosphere is known as the extraterrestrial radiation [41]. The variation in its value throughout the year is primarily due to Earth's changing position relative to the sun [5, 46]. The model proposed by Spencer for calculating the extraterrestrial radiation is given by [41, 44]:

$$\begin{aligned} I_0 = I_{\text{SC}} \cdot \big[1.00011 + 0.034221\cos(x) + 0.00128\sin(x) \\ -0.000719\cos(2x) + 0.000077\sin(2x)\big] \end{aligned} \tag{2.1}$$

where $I_{SC} = 1366.1\,\mathrm{Wm}^{-2}$ and for any day of the year $x = \frac{360°}{365}(\mathrm{DOY} - 1)$. Figure 2.2 displays the variation in extraterrestrial radiation throughout the year. The extraterrestrial irradiance on a horizontal surface is given by [30]:

$$H_0 = I_0 \cdot \cos\theta \tag{2.2}$$

where θ is the sun zenith angle.

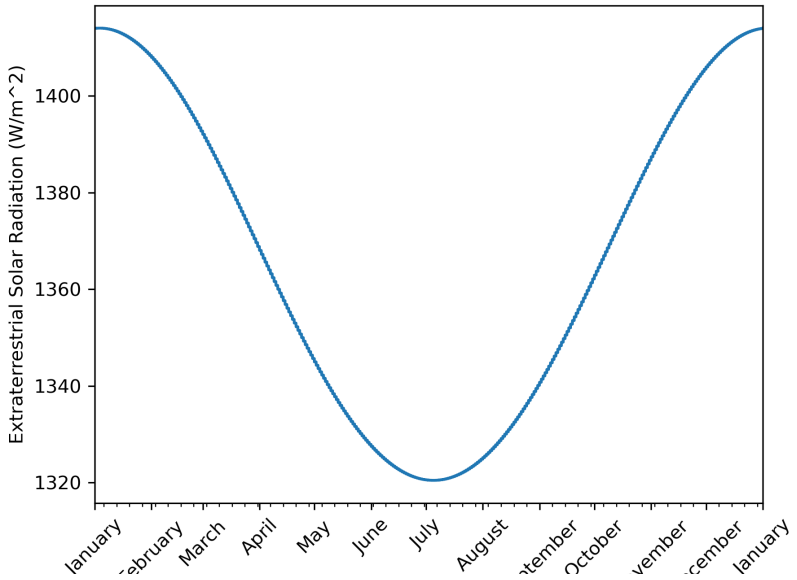

Figure 2.2: Variation in extraterrestrial radiation throughout different times of year

2.2.3 Solar radiation on Earth's surface

Understanding the nature of solar radiation as it reaches the surface of the Earth is important in this work. This section is divided into two parts. First, we introduce the components of solar radiation that reach a horizontal surface on Earth in Section 2.2.3.1. This includes Global Horizontal Irradiance (GHI) and its components: direct or beam horizontal irradiance (BHI) and diffuse horizontal irradiance (DHI). Following this, in Section 2.2.3.2, we present the specific spectrum of solar radiation that is vital for plant growth: the photosynthetically active radiation (PAR).

2.2.3.1 Global, direct and diffuse irradiance

Extraterrestrial radiation is reduced as it travels through Earth's atmosphere and as a result, the radiation level measured at the top of the atmosphere serves as a maximum limit that is typically not achieved by radiation reaching a horizontal surface on the ground, except in rare instances involving multiple cloud reflections [5, 46]. Global horizontal irradiance (GHI) is the total amount of irradiance measured on a horizontal surface on the surface of the earth. The two components of GHI are the direct or beam horizontal irradiance (BHI) and the diffuse horizontal irradiance (DHI). The relationship between these components is mathematically represented as [5]:

$$GHI = BHI + DHI \tag{2.3}$$

As a result, we are looking at two different sources of irradiance. The direct irradiance from the sun's position in the sky and the diffuse irradiance originating from the entire sky hemisphere around the receiver surface and hence without a defined direction [32, 39]. Solar irradiance is expressed in watts per square meter W/m^2.

2.2.3.2 Photosynthetically active radiation

Photosynthetically active radiation (PAR), refers to the specific spectrum of radiation ranging between 400 to 700 nm which is utilized by plants during the process of photosynthesis [46]. Photosynthetically active radiation can be quantified in energy units as W/m^2 or in photon units as $\mu mol/m^2/s$ [14]. Photosynthetic photon flux density (PPFD) can therefore be defined as the photon flux density in the 400-700 nm spectrum [14]. The conversion between the two units, within the 400 to 700 nm spectrum, can be achieved by multiplying W/m^2 by 4.57 and converting $\mu mol/m^2/s$ to W/m^2 involves dividing the photon unit by 4.57 [45].

PAR can be divided into two distinct components [13]: direct and diffuse, and this division can be represented mathematically as:

$$PAR_{\text{total}} = PAR_b + PAR_d \tag{2.4}$$

where PAR_b represents the direct component of PAR, and PAR_d denotes the diffuse component of the total PAR. Specifically, PAR_b represents the fraction of beam or direct horizontal irradiance (BHI) falling within the wavelength range of 400 to 700

nm, and PAR_d indicates the portion of diffuse horizontal irradiance (DHI) within the same spectral range.

2.3 Shade Modeling

The understanding of shade and light has very important applications in the context of urban planning, architecture, agriculture and solar power plants. Several approaches have been developed to model shading on a receiver surface caused by an obstacle between the surface and the light source. In the context of shade modeling , the receiver surface refers to any surface designed to capture or utilize solar irradiance. An obstacle in this context is any object that has the potential to cast a shadow on the receiver surface.

In Section 2.3.1, the concept of shading factor is introduced. In Section 2.3.2, we go though some methodologies that have been introduced in the literature for calculating shading factors and their applications in an agrivoltaic context.

2.3.1 Shading factors

A suitable and commonly used measure for the amount of shade caused by an obstacle on a receiver surface is the shading factor. Direct shading factor denotes the percentage of the receiver surface that is covered by shade [49] and diffuse shading factor represents the proportion of diffuse irradiance on the receiver surface that is diminished due to shading [39].

The amount of global irradiance on a shaded horizontal surface, GHI_s can be formulated as [38]:

$$GHI_s = BHI \cdot (1 - f_b) + DHI \cdot (1 - f_d) \tag{2.5}$$

where f_b is the shading factor for the direct component of the irradiance and f_d stands for the shading factor for diffuse irradiance. With respect to the photosynthetic active radiation (PAR), this relation can be expressed as:

$$PAR_s = PAR_b \cdot (1 - f_b) + PAR_d \cdot (1 - f_d) \tag{2.6}$$

where PAR_b and PAR_d represent the direct and diffuse component of the total PAR respectively as discussed in Section 2.2.3.2.

2.3.2 Shading factor calculation methods & Their application in AV systems

In the following, we explore two distinct methodologies from the literature for determining shading factors, each employing a different projection approach to account for obstacles. The first method projects the obstacle from the sun's perspective onto the receiver surface. The second method takes the perspective of the receiver surface, projecting the obstacle onto a hemispherical dome representing the sky.

Following the first method of projection from the sun to the receiver, a graphical approach to evaluating the amount of shade on a surface is to view the objects obstructing the light source as polygons defined by their vertices. After projecting the obstacle along the direction of sunlight on the receiver surface, the area of the shaded part can be graphically calculated by counting the number of points or pixels in the shade. The shading factor for direct irradiance is then given by the ratio between the number of pixels in the shade and the total number of pixels on the receiver surface [32, 39, 49]. Continuing with the sun-to-receiver projection technique, Cascone et al. [9] proposed a method for calculating the shading factor under complex boundary conditions. Their method is based on projecting the vertices of the obstacles in the direction of the sunlight onto the receiver plane and defining the shadow by the projected vertices. The shading factor for the direct irradiance is calculated by the ratio of the area of the projected polygon and the total area of the receiver surface.

The calculation of diffuse irradiance on an inclined surface involves integrating the radiance distribution from the portion of the sky visible to that surface [26, 9].

In line with the second method of projecting from the receiver surface to the sky, Quaschning et al. [38] introduced a method for evaluating the amount of direct and diffuse irradiance on a shaded surface. For calculating the direct shading factor, the vertices of the obstacle are projected onto the sky hemisphere from the direction of an observer point on the receiver surface. The shading at this observer point is determined based on whether the sun is positioned within the projected polygon. For the direct shading factor, a binary evaluation is used: it is assigned a value of one if the sun is within the projected polygon, indicating shading, and zero if the sun is outside, indicating no shading. This method focuses on a single point assessment on the receiver surface. Additionally, they computed the diffuse shading factor by the ratio between the double integral of radiance over the shaded area of the sky

hemisphere and the total amount of diffuse irradiance. It is important to note that these calculations are specifically developed for an individual observer point on the receiver plane [38].

To investigate the interaction between photovoltaic systems and crops within agrivoltaic setups, Campana et al. [8] and Zainali et al. [8] both utilized the sun-to-receiver projection method for their shading calculations. This approach was used in their efforts to model the distribution of crop relevant light in an agrivoltaic context. Campana et al. [8] introduced an optimisation model for agrivoltaic systems using vertically mounted, bifacial photovoltaic modules. They estimated the effective photosynthetically active radiation (PAR) received by crops by taking into account both the diffuse and direct components of PAR and the shadows cast by the rows of bifacial PV modules. Zainali et al. [50] constructed mathematical models in Matlab® to compute the shading factors, for both direct and diffuse components, in three distinct AV system configurations and assessed the distribution of PAR at ground level.

Adapting the second method of projection, from the receiver surface to the sky, Amaducci et al. [3] presented a model that computes both direct and diffuse radiation at ground level. This model was utilized to run simulations comparing the yield of maize in agrivoltaic (AV) systems with the yield in open fields in Northern Italy.

2.4 Methods for estimating photosynthetically active radiation

Although crucial, a worldwide system for the measurement of photosynthetically active radiation (PAR) is still lacking, despite its fundamental role in models of photosynthesis for land-based ecosystems [14, 33]. Additionally, the scarcity of observation stations that measure the diffuse fraction of PAR underscores the necessity for models to estimate these values [13]. Our aim is to focus on simple empirical models that use commonly available measurements such as GHI and DHI to estimate the total PAR and its diffuse fraction under all sky conditions.

Empirical models, which estimate PAR using meteorological parameters like global solar radiation or the clearness index, are the most commonly documented method in literature [33]. However, most models are specifically tailored to the conditions of

the original study site or to similar climates, necessitating modifications for broader applicability [33].

The models developed by Foyo-Moreno et al., which were validated at sites with different climatic characteristics from the original sites of development, present an exception to this trend [33, 14, 13]. The model, developed for estimating total photosynthetically active radiation (PPFD), uses the solar zenith angle, extraterrestrial horizontal irradiance and global horizontal irradiance [14]. The model developed to estimate the diffuse fraction of the photosynthetic photon flux density uses the solar zenith angle, extraterrestrial horizontal irradiance and diffuse horizontal irradiance as input data [13].

Approximately 45% of the direct solar energy at the Earth's surface falls within the photosynthetically active wavelength range [24]. However, when considering the sum of direct and diffuse radiation, the average percentage of energy in the PAR region increases to about 50%. This increase is attributed to the higher concentration of this wavelengths in diffuse radiation [24]. It is therefore feasible to approximate the value of PAR as a fraction of the total global horizontal irradiance.

In their study of the relationship between PPFD and GHI at a site in southeastern Spain, Foyo-Moreno et al. [14] observed that the ratio between PPFD and GHI varies, ranging from 1.52 to 2.39 μmol J^{-1}. The site is characterised by significant seasonal temperature variations, resulting in cool winters and hot summers [14]. They found that, on average, the ratio stands at 1.95 ± 0.12 (μmol J^{-1}) [14]. Hu et al. [19] reported the mean values for this ratio ranging from 1.75 ± 0.12 to 2.30 ± 0.15 (μmol J^{-1}) across China. The highest values were recorded in tropical regions, while the smallest value was noted at the Luancheng site, characterized by low humidity and a high concentration of fine aerosols [19]. Jacovides et al. [23] documented an average annual value of 1.995 ± 0.032 μmol J^{-1} for the ratio, based on data collected in Athens, Greece. The ratios ranged from 1.989 ± 0.028 μmol J^{-1} in summer [23] to 2.006 ± 0.032 μmol J^{-1} in winter.

In their study of the ratio between diffuse photosynthetic photon flux density (PPFD$_d$) and diffuse horizontal irradiance (DHI), Foyo-Moreno et al. [13] reported variations in this ratio from 1.86 to 2.48 μmol J^{-1}, with an average of 2.19 ± 0.13 μmol J^{-1}, based on data from a site in southeastern Spain. Based on data gathered at Athens, Greece, Jacovides et al. [23] observed that the seasonal ratios ranged from 2.298 ± 0.27 μmol J^{-1} in winter to 2.538 ± 0.22 μmol J^{-1} in summer, with an annual mean of 2.434 ± 0.26 μmol J^{-1} [23].

These findings underscores the impact of geographical and seasonal factors on the PPFD/GHI and $PPFD_d$/DHI ratios. Such variability highlights the necessity for adaptations of models to accurately capture these dynamic relationships.

Chapter 3

Method & Data

3.1 Overview

The methodology for modeling the distribution of light and shadow on the ground caused by a photovoltaic structure with a one-axis tracking system in this project is divided into two main steps. Initially, the focus is on determining the direct and diffuse shading factors. This is followed by the second step, which involves estimating the direct and diffuse photosynthetic photon flux density (PPFD). This estimation utilizes commonly available radiation data, including global horizontal irradiance (GHI) and diffuse horizontal irradiance (DHI).

In Section 3.2, the methods and procedures for calculating the direct and diffuse shading factors are described. Subsequently, in Section 3.3, the approaches for estimating both the direct and diffuse components of PPFD are explained. In Section 3.4, a metric for assessing the uniformity of light distribution is introduced. Lastly, Section 3.5 presents the data employed in this work.

3.2 Shading factor calculation

Section 3.2.1 outlines the definition and formulas required for computing the direct and diffuse shading factors, following the approach proposed by Cascone et al. [9].

Next, Section 3.2.2 provides a detailed explanation of the process used to calculate these shading factors in agrivoltaic systems with single-axis tracker photovoltaic (PV) structures.

3.2.1 Direct and diffuse shading factors: definitions & formulas

To compute the total radiation received on a surface potentially affected by shadows, we apply Equations 2.5 and 2.6. This involves determining the shading factors for both direct and diffuse radiation. The methodology for calculating the direct shading factor is detailed in Section 3.2.1.1, while the approach for the diffuse shading factor is explained in Section 3.2.1.2.

3.2.1.1 Direct shading factor

As mentioned in Section 2.3.1, the shading factor for the direct irradiance is defined as the ratio between the shaded area of the receiver surface and the total area of that surface [9]:

$$f_b = \frac{A_s}{A_r} \tag{3.1}$$

where A_r is the total area of the analyzed receiver surface and A_s is area of the shaded portion of that surface. The direct shading factor depends on the position of the sun and on the configuration of the receiver-obstacle system [9].

3.2.1.2 Diffuse shading factor

The diffuse shading factor for a receiver surface is the function of the portion of the sky hemisphere around the surface that is visible to it in the presence of an obstacle [9]. A suitable method for evaluating the diffuse irradiance from the sky on a tilted surface involves integrating the radiance across the visible sky hemisphere for that surface [26]. The irradiance, δI from a small segment of the sky on a surface is given by

$$\delta I = R_{\gamma\alpha} \cos(\beta) \delta\Omega$$

where $R_{\gamma\alpha}$ is the radiance of a segment of the sky at elevation α and azimuth γ in $W/(m^2 sr)$ [26]. Here, β is the angle between the segment of the sky and the surface's normal, and $\delta\Omega$ is the solid angle in steradians (sr). The solid angle can mathematically be formulated as $\delta\Omega = \cos(\alpha)\delta\alpha\delta\gamma$ [9]. Hence, the diffuse irradiance, I_d, can be calculated by a double integral [9]:

$$I_d = \int_{\alpha=0}^{\frac{\pi}{2}} \int_{\gamma=0}^{2\pi} R_{\gamma\alpha} \cos(\beta) \cos(\alpha)\, d\alpha\, d\gamma$$

For a horizontal surface $\beta = \frac{\pi}{2} - \alpha$ and the above formula can be rewritten as [38]:

$$I_{d,h} = \int_{\alpha=0}^{\frac{\pi}{2}} \int_{\gamma=0}^{2\pi} R_{\gamma\alpha} \sin(\alpha) \cos(\alpha)\, d\alpha\, d\gamma$$

Positioning an observer at every point on the sky hemisphere, the segment of the receiver surface that is visible to the observer is the same portion of the receiver surface that can be illuminated by that segment of the sky. The section of the sky that is not visible to the receiver surface therefore matches the shading factor for direct radiation [9]. Consequently, the shading factor for diffuse radiation is expressed as:

$$f_d = \frac{\int_{\alpha=0}^{\frac{\pi}{2}} \int_{\gamma=0}^{2\pi} f_b(\alpha,\gamma) R_{\gamma\alpha} \cos(\beta)\, d\Omega}{\int_{\alpha=0}^{\frac{\pi}{2}} \int_{\gamma=0}^{2\pi} R_{\gamma\alpha} \cos(\beta)\, d\Omega}$$

By discretising the sky hemisphere into $n \times m$ angular segments, with n segments in elevation (α) ranging from 0 to $\frac{\pi}{2}$ and m segments in azimuth (γ) ranging from 0 to 2π, and assuming an isotropic radiance distribution, where $R_{\alpha\gamma}$ is constant for all α and γ, the double integral can be numerically approximated as [9]:

$$f_d = \frac{\sum_{i=1}^{n} \sum_{j=1}^{m} f_{b,ij}(\alpha_i, \gamma_j) \cos(\beta_{ij}) \cos(\alpha_i) \Delta\alpha\Delta\gamma}{\sum_{i=1}^{n} \sum_{j=1}^{m} \cos(\beta_{ij}) \cos(\alpha_i) \Delta\alpha\Delta\gamma} \tag{3.2}$$

For a horizontal receiver surface, using the fact that $\beta = \frac{\pi}{2} - \alpha$ and $\cos(\beta) = \sin(\alpha)$, the expression can be simplified:

$$f_{d,h} = \frac{\sum_{i=1}^{n} \sum_{j=1}^{m} f_{b,ij}(\alpha_i, \gamma_j) \sin(\alpha_i) \cos(\alpha_i)}{\sum_{i=1}^{n} \sum_{j=1}^{m} \sin(\alpha_i) \cos(\alpha_i)} \tag{3.3}$$

3.2.2 Shading factor calculation for single-axis tracker agrovoltaic systems

In this section, we provide a comprehensive methodology for determining shading factors within agrovoltaic systems. The primary focus is on a photovoltaic structure equipped with a single-axis tracker system. The arrangement of solar panel rows in this setup and their representation in our shading model are described in Section 3.2.2.1. Additionally, we outline various coordinate systems and angles essential for calculating shading factors in the context of agrovoltaics in Section 3.2.2.2. The algorithm for computing solar position angles is presented in Section 3.2.2.3, while Section 3.2.2.4 discusses how to derive the optimal rotation angle for a single-axis tracker system with arbitrary orientation. Furthermore, Section 3.2.2.5 describes the process for adjusting the position of the photovoltaic modules, and Section 3.2.2.6 presents the technique to determine the shadows' shapes, which is crucial for calculating direct shading factors. A visual representation of the entire process of direct and diffuse shading factor calculations at each time step in an agrovoltaic context is provided in Figures 3.1 and 3.2.

3.2.2.1 Configuration of AV system

For the purposes of this project, it is essential to understand the configuration of AV system in our model. As illustrated in Figure 3.3, Photovoltaic (PV) solar panels are arranged in parallel rows, with each row represented as a rectangular surface elevated above the ground and defined by the rectangle's four vertices. The horizontal positions of these four vertices for each row are defined as follows::

$$
\begin{aligned}
p_1 &= (x_0, y_0, h) \\
p_2 &= (x_0, y_0 + \mathrm{l}, h) \\
p_3 &= (x_0 + \mathrm{w}, y_0 + \mathrm{l}, h) \\
p_4 &= (x_0 + \mathrm{w}, y_0, h)
\end{aligned}
$$

Here, w represents the width, l is the length, and h is the height of the row of solar panels. The coordinates x_0, y_0 designate the initial position of each row in the xy-plane.

In horizontal single-axis tracking AV system, the primary subject of this project, the horizontal axis of rotation is typically north-south oriented and the panels in

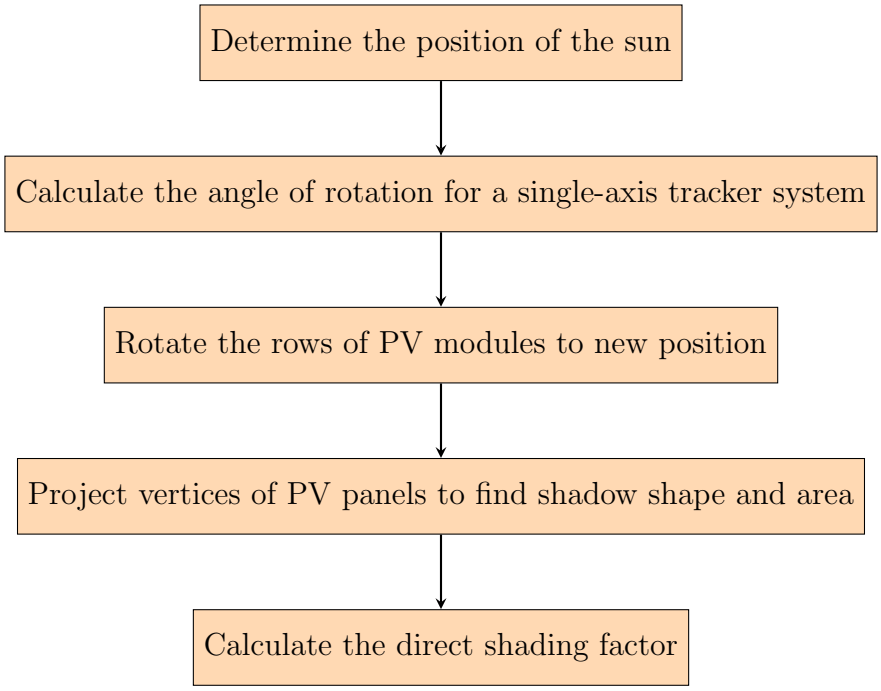

Figure 3.1: The process for calculating direct shading factors at each time step in agrovoltaic systems.

each row rotate around the fixed axis throughout the day, aiming to follow the sun's movement from east to west. However, it is noteworthy that in practice, the panels' rotation angle has a defined maximum limit.

The spacing between neighbouring rows is determined by the distance between their respective tracker axes and is referred to as the pitch. Shade calculations are conducted for a horizontal area situated at ground level between the panel rows, as shown in Figure 3.3. This area's length matches the PV panel rows' length, while its width is equivalent to the pitch.

For a more detailed assessment of the distribution of light and shade on the ground, the area between the rows depicted in Figure 3.3, is divided into 1 m $\times$ 1 m cells and the shading calculations are carried out for each individual cell.

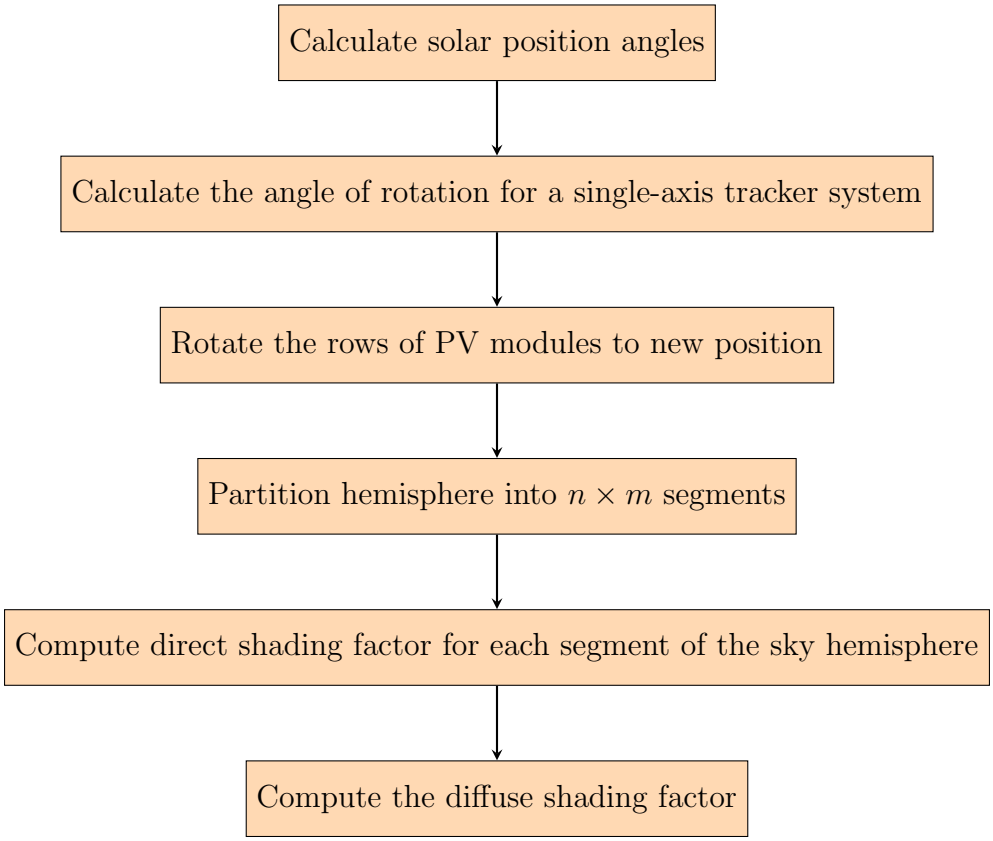

Figure 3.2: The process for calculating diffuse shading factors at each time step in agrovoltaic systems.

3.2.2.2 Coordinate systems & angles

It is important to define and clarify the relevant coordinate systems and angles that are used in this work. In this work we refer to two different coordinate systems. The primary system is a global Cartesian coordinate system where the x-axis aligns with the east, the y-axis points to north, and the z-axis stands perpendicular to the xy-plane. Azimuth angle, ranging from 0° to 360°, is determined in a clockwise fashion from the north, rotating around the global z-axis. Elevation angle represents the upwards angle of inclination from the horizontal plane, with values ranging from 0° to 90°.

The second coordinate system, referred to as the tracker Cartesian coordinate system,

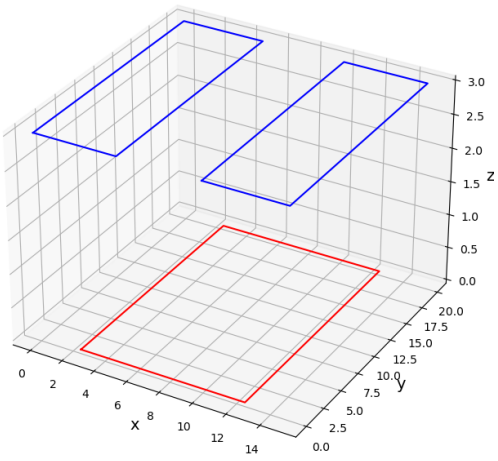

(a) Elevated solar panels are depicted as two blue rectangles. The Red rectangle represents the ground-level area used for shade calculations.

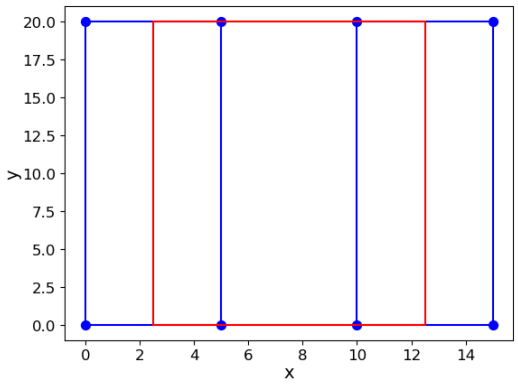

(b) Overhead view of two solar panel rows with vertices marked with blue points and a red rectangle indicating the ground-level area used for shade calculation.

Figure 3.3: Illustrating both side and overhead views of two rows of solar panels, each 20 m long, 5 m wide and elevated 3 m above the ground with a 10 m spacing (pitch) between the two rows and displaying ground-level area that is used for shade calculations.

is oriented based on the position and orientation of a specific tracker system. The tracker coordinate system is obtained by rotating the global coordinate system by tracker's axis azimuth around the z-axis and axis elevation angle around the x-axis [4, 28]. Given tracker axis azimuth angle γ_a and tracker axis elevation angle σ_a, the conversion of a vector $\vec{a}$ in the global coordinate system to $\vec{a}\,'$ in the tracker coordinate system is accomplished by first rotating by the axis azimuth γ_a around the z-axis, followed by a counterclockwise rotation around the x-axis by the axis elevation σ_a [4]:

$$\vec{a}\,' = R_x R_z \vec{a} \tag{3.4}$$

with:

$$R_x = \begin{bmatrix} 1 & 0 & 0 \\ 0 & \cos\sigma_a & -\sin\sigma_a \\ 0 & \sin\sigma_a & \cos\sigma_a \end{bmatrix}, \quad R_z = \begin{bmatrix} \cos\gamma_a & -\sin\gamma_a & 0 \\ \sin\gamma_a & \cos\gamma_a & 0 \\ 0 & 0 & 1 \end{bmatrix} \tag{3.5}$$

In the resulting tracker coordinate system, the x-axis (t_x) is horizontal and orthogonal

to the tracker axis, the y-axis (t_y) runs parallel to the tracker axis and points in the direction of the tracker's axis azimuth, and the z-axis (t_z) is determined by the right-hand rule as the cross product of t_x and t_y [4].

Although the angles γ_a and σ_a are measured clockwise, the conversion of vectors from global to tracker coordinate system involves counterclockwise rotations. The counterclockwise rotations is due to the angles γ_a and σ_a serving as the basis for converting coordinates from global to tracker coordinate system. Therefore, their negatives are utilized in the transformation of vectors from global to tracker coordinates [4]. It noteworthy that when the tracker's axis azimuth and axis elevation angles are zero, the tracker coordinate system coincides with the global coordinate system.

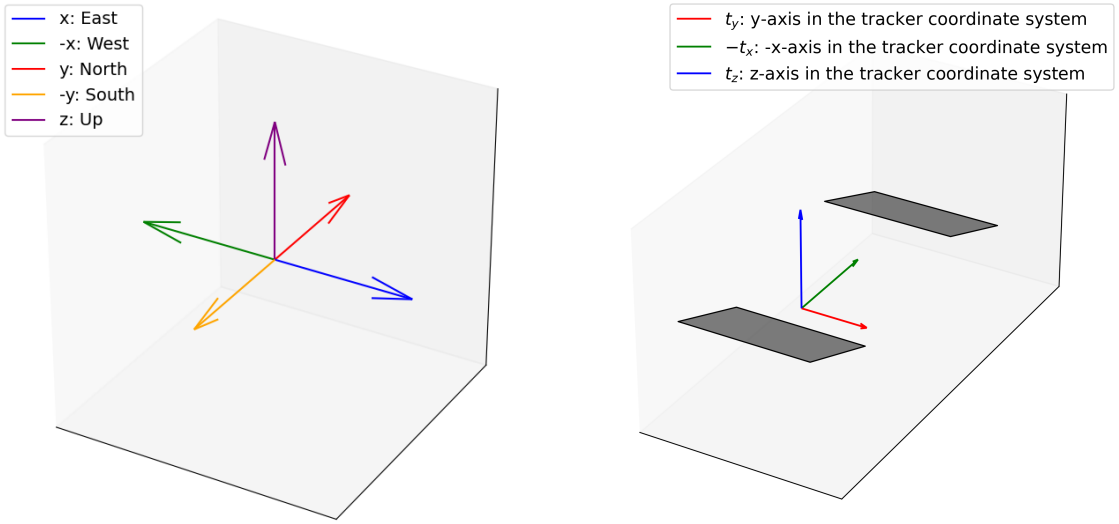

(a) Illustrating the global Cartesian coordinate system with the x-axis oriented eastward, the y-axis oriented northward, and the z-axis oriented upward

(b) Depicting the tracker's Cartesian coordinate system, set with t_x as the horizontal x-axis, orthogonal to the tracker axis, t_y as the y-axis parallel to the tracker axis and directed towards its azimuth, and t_z as the z-axis, perpendicular to both according to the right-hand rule.

Figure 3.4: Illustrating the global and tracker's Cartesian coordinate systems. The primary system is a global Cartesian coordinate system where the x-axis aligns with the east, the y-axis points to north, and the z-axis stands perpendicular to the xy-plane. The tracker coordinate system is obtained by rotating the global coordinate system by tracker's axis azimuth around the z-axis and axis elevation angle around the x-axis.

3.2.2.3 Position of the sun

The solar position angles are calculated using the solar position algorithm (SPA) of the pvlib module in Python [18] which by default utilizes an implementation of the National Renewable Energy Laboratory (NREL) SPA algorithm outlined by Reda et al. [40]. The position of the sun is primarily a function of the location described by its latitude, longitude and elevation as well as the date and time.

3.2.2.4 Angle of rotation for single-axis trackers

Single-axis trackers allow solar panels to rotate around one axis, namely the y-axis in the tracker's coordinate system as illustrated in Figure 3.5. Because of this singular axis of rotation, the trackers can not always point the panel directly towards the sun. The direct component of the irradiance collected by the solar panels is maximized when the angle of incidence, which is the angle between incoming direct sunlight and the solar panel's normal, is minimized [4]. It should be noted that the tracker rotation angle is defined as a counterclockwise angle around the y-axis in the tracker's coordinate system (see Figure 3.4b). To achieve this ideal angle ω_{ID}, the tracker's rotation is adjusted to align with the sun's projected position on the tracker plane of rotation [4]. The trackers plane of rotation is perpendicular to the tracker axis of rotation as shown in Figure 3.6. The projection of the solar coordinates onto the tracker plane of rotation is achieved by transforming the solar vector from global coordinates into the tracker coordinate system using Equation 3.4.

Given the solar elevation angle α_s and solar azimuth angle γ_s, the solar vector can be expressed in the global Cartesian coordinates in terms of the spherical coordinates with [4]:

$$\mathbf{s} = \begin{cases} x_s = \sin(\gamma_s)\cos(\alpha_s) \\ y_s = \cos(\gamma_s)\cos(\alpha_s) \\ z_s = \sin(\gamma_s) \end{cases} \tag{3.6}$$

The solar vector, when converted into the tracker coordinate system using Equation (3.4), is represented as:

$$\mathbf{s}' = \begin{cases} x'_s = x_s \cos\gamma_a - y_s \sin\gamma_a \\ y'_s = x_s \sin\gamma_a \cos\sigma_a + y_s \cos\gamma_a \cos\sigma_a - z_s \sin\sigma_a \\ z'_s = x_s \sin\gamma_a \sin\sigma_a + y_s \cos\gamma_a \sin\sigma_a - z_s \cos\sigma_a \end{cases} \tag{3.7}$$

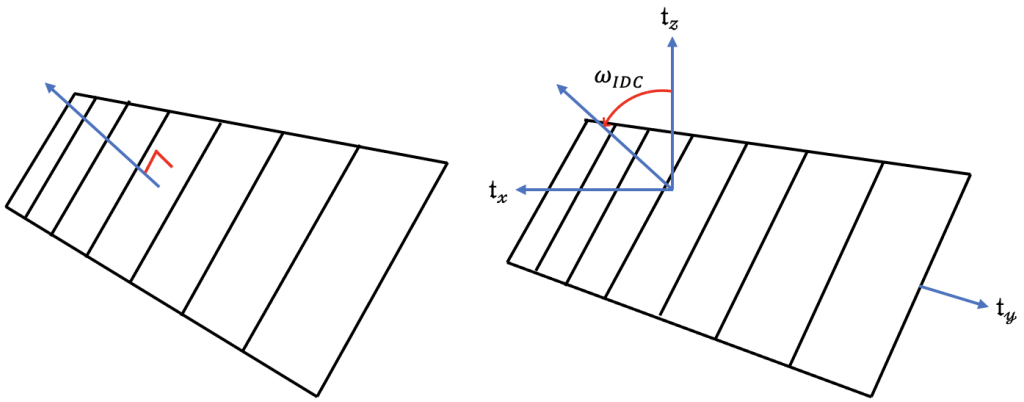

Figure 3.5: Illustrating the tracker rotation angle ω_{IDC} in a single-axis tracker system. The rotation in right-handed around the y-axis in the tracker coordinate system. Assuming a north-south orientation of the tracker axis, the angle shown in the illustration represents a positive eastward rotation.

Since the components x'_s and z'_s represent the projection of the sun's position on the tracking rotation plane (see Figure 3.6), the optimal angle ω_{ID} for aligning the collector surface with this projected position is given, as evident from Figure 3.6, by [4, 28]:

$$\tan \omega_{ID} = \frac{x'_s}{z'_s} \tag{3.8}$$

When the sun is low in the sky, the rotation angle of the tracker may exceed $\pm 90°$. To account for this, the ideal angle is defined as:

$$\omega_{ID} = \text{atan2}(x'_s, z'_s) \tag{3.9}$$

This formulation provides an extended range of $(-180°, +180°]$ in contrast to the expression $\arctan \frac{x'_s}{z'_s}$ which is restricted to a narrower interval of $(-90°, +90°)$ [4].

Shading on PV panels diminishes the electrical power output [28]. Back-tracking is a tracking motion strategy that aims to eliminate mutual shading among PV arrays. It is achieved by adjusting the ideal rotation angle of the trackers such that the shadow from a row of panels falls just on the border of the the neighboring row [28]. This strategy ensures that inter-row shading is avoided at the cost of reducing the

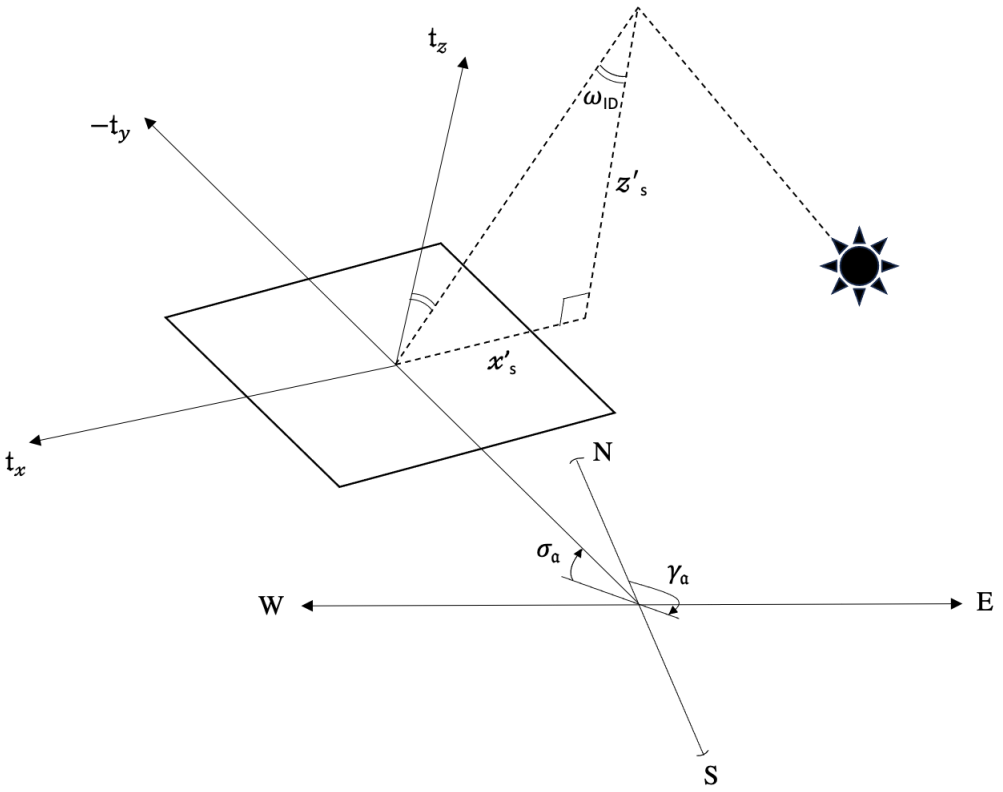

Figure 3.6: The ideal tracker angle ω_{ID}: the tracker's rotation is adjusted to align with the sun's projected position on the tracker plane of rotation defined by t_x and t_z. The ideal tracker angle ω_{ID} is given by $\tan\omega_{ID} = \frac{x'_s}{z'_s}$.

angle of incidence from optimality. Lorenzo et al. [28] presented an overview of the back-tracking geometry for different tracking systems. Our focus in this work is on the back-tracking adjustment for trackers with single axis where rows are aligned without a vertical offset.

Figure 3.7 illustrates the geometry of a single axis tracker system, the ideal tracking angle ω_{ID}, the back-tracking correction angle ω_C and the corrected ideal tracker rotation angle ω_{IDC}. Considering the right triangle ABD:

$$\cos\omega_{ID} = \frac{AB}{AD}$$

and considering right triangle ABC:

$$\cos \omega_C = \frac{AB}{AC}$$

Given the fact that $AC = \frac{w_r}{2}$ and $AD = \frac{p}{2}$:

$$\cos \omega_C = \frac{\cos \omega_{ID}}{GCR}$$

Here, GCR represents the ground coverage ratio, defined as the quotient of the width of the row of solar panels w_r to the spacing between two parallel tracker axes p. For effective backtracking, the sign of the back-tracking correction angle should oppose that of the ideal tracking angle. Thus, the adjusted tracking angle is given by [28] [4]:

$$\omega_{IDC} = \omega_{ID} - \text{sign}(\omega_{ID}) \cos^{-1}\left(\frac{\cos \omega_{ID}}{GCR}\right) \tag{3.10}$$

Figure 3.8 displays comparative plots of the daily variations in the angle of rotation for a horizontal single-axis tracker system in Lund, Sweden. It illustrates scenarios both with and without backtracking, over a day in September.

3.2.2.5 Rotation of the rows of photovoltaic panels

Rotation around a single axis refers to a right-handed rotation specifically around the y-axis within the tracker's coordinate system. When the tracker axis is horizontal and perfectly north-south oriented, the y-axis of the tracker coordinate system coincides with the global y-axis. To rotate the vertices of a rectangular PV panel around the y-axis by an angle ω_t, the following steps are taken [31]. Considering the panel vertices $P_i(x_i, y_i, z_i)$ for $i \in \{1, 2, 3, 4\}$:

1. **Calculate the center of the rectangle:**

$$\mathbf{C} = \frac{1}{N} \sum_{i=1}^{N} P_i$$

   where $N = 4$ is the number of vertices.

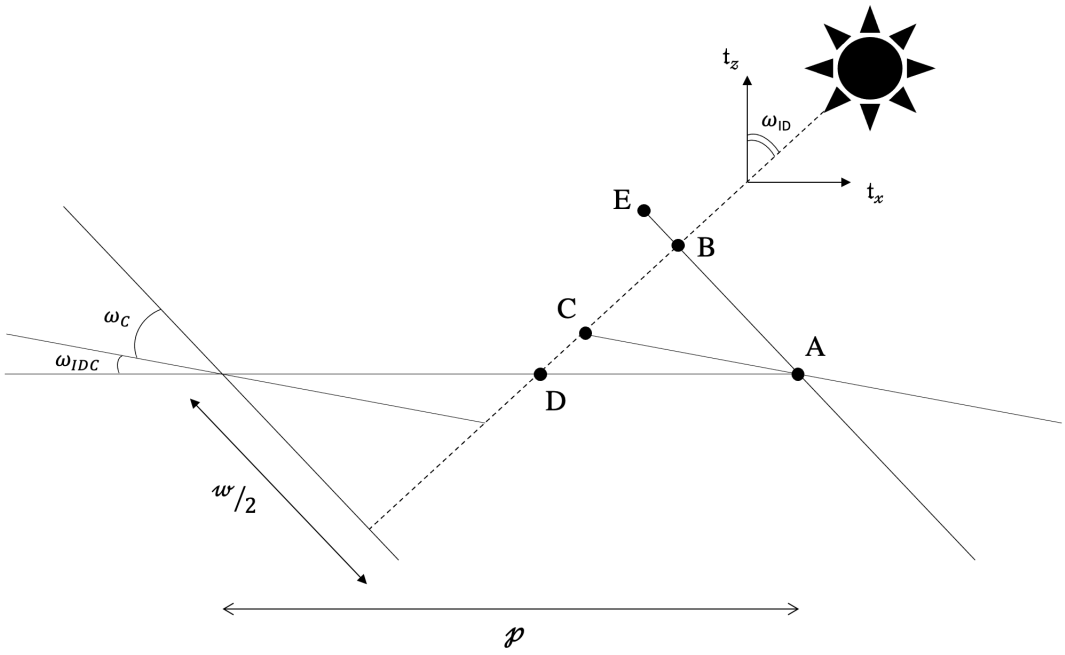

Figure 3.7: A side view of to parallel solar arrays with single axis tracker. Position E shows the placement of the solar panel rows without back-tracking and position C depicts their position after back-tracking correction is applied. The spacing between the two neighboring tracker axes is p and the width of each row of panels is w.

2. **Translate the rectangle to the origin**: For each vertex (x_i, y_i, z_i) where $i \in \{1, 2, 3, 4\}$:

$$P_i' = \begin{cases} x_i' = x_i - c_x \\ y_i' = y_i - c_y \\ z_i' = z_i - c_z \end{cases}$$

3. **Rotate the rectangle about the y-axis**: For each vertex (x_i', y_i', z_i') where $i \in \{1, 2, 3, 4\}$:

$$\begin{bmatrix} x_i'' \\ y_i'' \\ z_i'' \end{bmatrix} = R_y(\omega_t) \begin{bmatrix} x_i' \\ y_i' \\ z_i' \end{bmatrix}$$

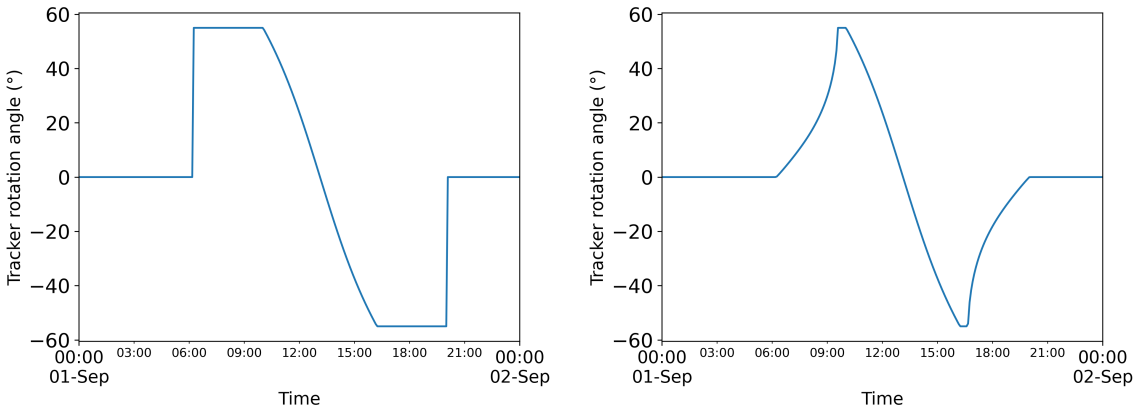

(a) Changes in the tracker's rotation angle corresponding to the sun's position throughout the day, Without Backtracking

(b) Changes in the tracker's rotation angle with the changes in the sun's position during the day, With Backtracking

Figure 3.8: This figure shows variations in the rotation angle of a horizontal single-axis tracker system on September 1st in Lund, Sweden. The comparison highlights the system's behavior both with and without backtracking. The tracker axis azimuth is set to zero, the ground coverage ratio (GCR) is 0.5, and the maximum angle is limited to 55 degrees.

where:

$$R_y(\omega_t) = \begin{bmatrix} \cos(\omega_t) & 0 & \sin(\omega_t) \\ 0 & 1 & 0 \\ -\sin(\omega_t) & 0 & \cos(\omega_t) \end{bmatrix}$$

4. **Translate back to the original position**: For each rotated vertex (x_i'', y_i'', z_i'') where $i \in \{1, 2, 3, 4\}$:

$$P_{\text{rotated},i} = \begin{cases} x_{\text{rotated},i} = x_i'' + c_x \\ y_{\text{rotated},i} = y_i'' + c_y \\ z_{\text{rotated},i} = z_i'' + c_z \end{cases}$$

3.2.2.6 Calculation of shadows

In order to calculate the shading factors for direct and diffuse irradiance, we need the area of the shaded portion of the analyzed surface on the ground beneath the PV structure. Consequently, we need the shape of the shadows projected onto that surface by the PV structure as obstacles [9]. For this purpose, the obstacles, represented

as rectangular rows of solar panels, are characterized by their vertices. Each vertex is projected in the direction of direct sun light onto the plane positioned on the ground beneath the panels. Thereby defining the shadow based on these projected vertices on this plane.

Given the solar elevation α_s and solar azimuth γ_s, the solar vector can be expressed in Cartesian coordinates in the global coordinate system as shown in Equation 3.6. The transformation of the solar vector from the global coordinate system to the tracker coordinate system is accomplished using Equation 3.4. Equation 3.7 represents the transformed solar vector, converted from the global coordinate system to the tracker coordinate system. This is particularly relevant when the tracker axis azimuth angle γ_a and axis elevation angle σ_a are not zero, resulting in the global coordinate system not aligning with the tracker coordinate system.

The normal vector to a generic plane with azimuth γ_p and elevation σ_p, where the y-axis is oriented northward and the x-axis is oriented eastward and the z-axis pointing upward, is given by:

$$\mathbf{n} = \begin{cases} x_n = \sin(\sigma_p)\sin(\gamma_p) \\ y_n = \sin(\sigma_p)\cos(\gamma_p) \\ z_n = \cos(\sigma_p) \end{cases} \tag{3.11}$$

and the equation of the line projecting a point $P = (x_0, y_0, z_0)$ on in the direction of sunlight is given by:

$$\mathbf{l} = \begin{cases} x_l = x_0 + x_s \cdot t \\ y_l = y_0 + y_s \cdot t \\ z_l = z_0 + z_s \cdot t \end{cases} \tag{3.12}$$

The intersection of the projective line with the receiver plane is found by plugging the line equation into the plane equation and solving for t:

$$t = -\frac{x_n x_0 + y_n y_0 + z_n z_0}{x_n x_s + y_n y_s + z_n z_s} \tag{3.13}$$

where x_s, y_s and z_s are the components of the solar vector.

For a horizontal receiver plane at ground level, oriented so that both azimuth γ_p and elevation σ_p are zero, and with a normal vector $\mathbf{n} = (0, 0, 1)$, Equation 3.13 simplifies to the following form:

$$t = -\frac{z_0}{z_s'} \tag{3.14}$$

Subsequent to obtaining the value of t, its insertion into the line equation yields the intersection point's coordinates:

$$P' = \begin{cases} x'_0 = x_0 + x_s \cdot t \\ y'_0 = y_0 + y_s \cdot t \\ z'_0 = z_0 + z_s \cdot t \end{cases} \tag{3.15}$$

To calculate the shape and area of the shadow cast by each row of solar panels, the four vertices of every row are projected onto a horizontal ground surface forming a shadow polygon. In situations where multiple rows are present, these shadow polygons may overlap with each other. The overall shadowed area, resulting from all the rows, is obtained by merging these overlapping shadow polygons [39, 50]. This concept is mathematically represented as:

$$A_s = \bigcup_{i=1}^{n} A_{s,i}$$

In this expression, A_s denotes the total shaded area, n signifies the total number of rows of solar panels, and $A_{s,i}$ represents the shadowed area produced by the i^{th} row of panels. The shaded portion of the reference area, which is the space between the rows of panels, is identified by the intersection of this combined shadow area with the reference surface.

3.2.2.7 Calculation of direct shading factor

The shading factor for direct radiation is calculated, using Equation 3.1, by dividing the area of the shaded portion of the reference surface with total area of the reference surface.

3.2.2.8 Calculation of diffuse shading factor

The portion of the sky hemisphere visible to the surface between the the two rows of panels changes at each time step as the panels adjust their position based on the sun's movement. The diffuse shading factor is therefore computed at each time step.

The sky hemisphere is partitioned into $n \times m$ sections by incrementing in steps of size $\frac{360}{n}^\circ$ in azimuth and $\frac{90}{m}^\circ$ in elevation. Each segment is specified by its unique combination of elevation and azimuth angles, which determine the position of the hypothetical sun in the sky. Vertices of PV panels are projected on the horizontal ground reference area to find shadow shape and area and compute the direct shading factor for each distinct combination of elevation and azimuth. Finally, the diffuse shading factor is computed using the formula presented in Equation (3.3).

3.2.2.9 Incorporation of diffuse shading factor tables

The calculation of the diffuse shading factor requires numerous computations at each time step. However, this process can be made more efficient by utilizing tables of pre-calculated diffuse shading factors for a specified configuration. Since the diffuse shading factors are independent of the sun's position, it is possible to compute the shading factors for a specific set of solar panel positions, defined by their range of rotation angles. Then, for the actual rotation angle that is calculated at each time step, the shading factor can simply be determined by interpolating between the values in the table, reducing the computational load.

This approach was implemented to enhance the efficiency of diffuse shading factor computations. Initially, diffuse shading factors were calculated for a range of tracker rotation angles, spanning from the negative to the positive maximum rotation angle with step sizes of one. Then, at each time step, the actual tracker angle was computed, and the diffuse shading factor was determined by interpolating between the available table values. A preliminary analysis revealed minor disparities between the interpolated and actual values. However, these discrepancies were found to be negligible, affirming the ability of the method to improve the computational efficiency.

3.3 Methodology for estimating photosynthetic photon flux density

To model the light relevant to crops in an agrivoltaic system, it is essential to quantify both the direct and diffuse components of photosynthetic photon flux density (PPFD). In this section, we present the methods employed in this study to estimate

total and diffuse PPFD using readily accessible radiation data. The amount of direct PPFD can then be calculated from these values using Equation (2.4).

To estimate the total and diffuse photosynthetic photon flux density (PPFD) in units of μmol $\mathrm{m}^{-2}\mathrm{s}^{-1}$, we utilize regression models developed by Foyo-Moreno et al. [14, 13], as discussed in Section 2.4. These models rely on the following expression for estimation [14, 13]:

$$PPFD = a \cdot \frac{Rad}{H_0} \cdot \cos\theta \tag{3.16}$$

With regression coefficient (a) set to $a = 2681 \pm 2\,\mu\mathrm{mol\,m^{-2}\,s^{-1}}$. The term Rad represents the global horizontal irradiance (GHI) when estimating the total PPFD, and it is substituted with diffuse horizontal irradiance (DHI) when estimating the diffuse PPFD. H_0 denotes the extraterrestrial global irradiance on a horizontal surface (Wm^{-2}) as given by Equation (2.2) and θ represents the solar zenith angle. Additionally, the ratio $\frac{GHI}{H_0}$ is known as the clearness index and is denoted by k_t. Equation (3.16) can be written as:

$$PPFD = a \cdot \frac{Rad}{H_0} \cdot \cos(\theta) = a \cdot \frac{Rad}{I_0 \cdot \cos(\theta)} \cdot \cos(\theta) = \frac{a}{I_0} \cdot Rad \tag{3.17}$$

where I_0 is the extraterrestrial radiation (Wm^{-2}) received on a plane normal to the direction of the sun and given by Equation (2.1).

The results of the previous studies on the ratio between PPFD and GHI, as well as diffuse PPFD and DHI were presented in Section 2.4. The reported results imply that these ratios can depend on both the geographical location and time of the year and therefore are not constant throughout the year. However, assuming that each ratio can be approximately represented by a fixed constant during the entire year, one can estimate total and diffuse PPFD by multiplying GHI and DHI by fixed factors.

In the calculation of extraterrestrial radiation using the Spencer model (Equation (2.1)), we observe seasonal variation in Figure 2.2. The model indicates that the radiation at the top of the atmosphere peaks at approximately $1414\,\mathrm{W/m^2}$ and reaches a minimum of around $1320.5\,\mathrm{W/m^2}$ over the course of a year. Consequently, when we consider the ratio of the constant 'a' in Equation (3.17) (valued at 2681 μmol $\mathrm{m}^{-2}\mathrm{s}^{-1}$) to extraterrestrial radiation (measured in $\mathrm{W/m^2}$), this ratio fluctuates between $1.9\,\mu$mol/J and $2.03\,\mu$mol/J during different times of year. By selecting a constant value of $2.1\,\mu$mol/J to represent this ratio, we essentially assign a slightly higher value to it

which is above the range suggested by the model in Equation (3.17). Consequently, this decision leads to an increased ratio of total PPFD to GHI and diffuse PPFD to DHI, compared to the ratios obtained from the models' calculations.

From another perspective, if we consider that approximately 46% of the total global horizontal irradiance (GHI) falls within the photosynthetically active wavelengths and use a conversion factor of $1\,\mathrm{W/m^2} \approx 4.57\,\mu\mathrm{mol/m^2/s}$ (for converting energy units to photon units as discussed in Section 2.2.3.2), we arrive at the conversion factor of $2.1\,\mu\mathrm{mol/J}$. The same reasoning can be applied for estimating the diffuse PPFD from diffuse global horizontal irradiance (DHI). However, in the context of the diffuse PAR, conversion from energy to photon units requires considering changes in diffuse PAR's spectral composition due the variation in the sky conditions. Neglecting this aspect and using the constant conversion factor of 4.57 for converting from energy to photon units can result in up to a 7% error in the calculated values in photon units [11].

In this work, our objective is to select a diverse range of locations with varying climates across Europe to evaluate the performance of the model (Equation (3.17)) for estimating total and diffuse PPFD. This approach is designed to understand how the models perform under different climatic conditions and to assess their adaptability to local environmental factors.

For each selected location, we begin by assessing the performance of the model in Equation (3.17) for estimating total PPFD using the regression coefficient a suggested by Foyo-Moreno et al. [14] ($a = 2681 \pm 2\,\mu\mathrm{mol\,m^{-2}\,s^{-1}}$). This step establishes a baseline performance, referred to as Model 1, without any location-specific training. Next, the model undergoes training on the dataset specific to each location to determine a location-specific coefficient a, resulting in Model 2. Model 2, incorporating the location-specific coefficient, is then evaluated against the testing dataset to compare its performance with Model 1. Additionally, we introduce Model 3, which estimates total PPFD using a general method of multiplying GHI by a conversion factor of $2.1\,\mu\mathrm{mol/J}$. This method represents a broader, less precise estimation technique. The performance of Model 3 is subsequently evaluated on the testing dataset to compare its effectiveness against Models 1 and 2.

We apply a similar approach to estimate diffuse PPFD. Initially, we evaluate Model A using the regression model Equation (3.17) for estimating diffuse PPFD and the regression coefficient a proposed by Foyo-Moreno et al. [13] ($a = 2681 \pm 2\,\mu\mathrm{mol\,m^{-2}\,s^{-1}}$). Then, we develop Model B through location-specific training and

compare its performance against Model A. Lastly, we introduce Model C, a less precise estimation method involving the multiplication of DHI by a conversion factor of 2.1 μmol/J. We assess the effectiveness of Model C and compare its performance to that of Models A and B on the testing datasets.

3.3.1 Goodness-of-fit measure

The performance of the models was evaluated using:

- Mean Absolute Error (MAE):

$$\text{MAE} = \frac{1}{n}\sum_{i=1}^{n}|y_i - \hat{y}_i|$$

- Mean Squared Error (MSE):

$$\text{MSE} = \frac{1}{n}\sum_{i=1}^{n}(y_i - \hat{y}_i)^2$$

- Root Mean Squared Error (RMSE):

$$\text{RMSE} = \sqrt{\frac{1}{n}\sum_{i=1}^{n}(y_i - \hat{y}_i)^2}$$

- Normalized Root Mean Squared Error (NRMSE) as a percentage:

$$\text{NRMSE (\%)} = \left(\frac{\text{RMSE}}{\bar{y}}\right) \times 100$$

- R-squared (R^2):

$$R^2 = 1 - \frac{\sum_{i=1}^{n}(y_i - \hat{y}_i)^2}{\sum_{i=1}^{n}(y_i - \bar{y})^2}$$

In these formulas:

- n is the number of observations.
- y_i represents the measured values.
- $\hat{y}_i$ represents the estimated values.
- $\bar{y}$ represents the average of the measured values.

3.4 Light distribution

As mentioned in Section 3.2.2.1, the area between the rows of panels shown in Figure 3.3 is discretised into smaller segments for a more detailed analysis of the distribution of light in the AV system. The light homogeneity index (LHI) is a metric for evaluating and comparing different AV systems based on the distribution of PPFD within the AV systems [50]. Its value is given by [50]:

$$LHI = 100 \cdot \left(1 - \left(\frac{\sqrt{\frac{1}{n-1}\sum_{i=1}^{n}(x_i - \bar{x})^2}}{\bar{x}}\right)\right) \tag{3.18}$$

Here, n represents the total number of discretized regions on the ground, x_i denotes the PPFD reaching the ground in each segment, factoring in shading from the AV system, and $\bar{x}$ is the average PPFD value across all segments. A light homogeneity index (LHI) of 100% indicates an even distribution of PPFD across the ground area, signifying a completely homogeneous light distribution.

3.5 Data

In the course of this work, we use three distinct datasets. The first dataset is used to assess the performance of models in estimating the total photosynthetic photon flux density (PPFD) across various locations in Europe. The second dataset is utilized for evaluating the performance of the models for estimating the diffuse photosynthetic photon flux density (PPFD_d) across different locations in Europe. Details about these datasets, downloaded from the Integrated Carbon Observation System (ICOS) Carbon portal, are provided in Section 3.5.1. The third group consists of typical

meteorological year (TMY) radiation data specifically for the sites of our agrivoltaic shade and light modeling. The data contains both total global horizontal irradiance (GHI) and diffuse global horizontal irradiance (DHI) measurements and is presented in Section 3.5.2.

3.5.1 ICOS data

In order to asses the performance of the models for estimating total photosynthetic photon flux density (PPFD) as detailed in Section 3.3, 7 different sites in Europe were chosen. The data contains half hourly measurements of total PPFD and short wave radiation (GHI). The chosen stations include Svartberget [34] and Hyltemossa [17] in Sweden, Soroe [22] in Denmark, Selhausen Juelich [42] in Germany, Puechabon [27] and Lamasquere [7] in France, and Castelporziano2 [12] in Italy.

To evaluate the performance of the models for estimating diffuse photosynthetic photon flux density ($PPFD_d$) as detailed in Section 3.3, 3 different sites in Europe were chosen. The datasets containing half hourly measurements of diffuse PPFD and diffuse horizontal irradiance (DHI) were downloaded from the Integrated Carbon Observation System (ICOS) Carbon portal. The selected stations include Voulundgaard [15] in Denmark, Gebesee [6] in Germany and Lamasquere [7] in France.

This collection of locations across Europe aims to provide a thorough and nuanced assessment of the models' performance in different parts of Europe. Figure 3.9 shows the available total and diffuse PPFD data for each station and Table 3.1 contains general information about each selected ICOS station.

The datasets contain level-2 quality controlled data. Additional quality assurance is implemented by excluding instances where the recorded diffuse PPFD exceeded the total PPFD in locations where diffuse PPFD measurements are available. Moreover, instances where irradiance measurements, GHI, DHI, total PPFD, or diffuse PPFD, are recorded as negative while the solar elevation angle is greater than zero, are set to zero values.

For a comprehensive assessment that captures seasonal variability, the training and testing datasets were carefully selected for each location. In cases where the data spanned less than two years or significant gaps were present within the available years, the data was arranged in consecutive four-week segments. Each segment was

then divided equally, the first two weeks were allocated for model training, and the latter two for testing. For locations with a close to complete two-year dataset, the model utilized one year's data for training and the other year's data for testing.

Table 3.1: The table provides general information about the ICOS stations and the data chosen for modeling both total and diffuse PPFD. The first part of the table presents details for seven stations selected for modeling total PPFD, while the second part focuses on three stations chosen for modeling diffuse PPFD.

Station	Coords. (Lat., Long.)	Elev. (m)	Mean An. Temp. (°C)	Mean An. Precip. (mm)	Mean An. Solar Rad. (W/m^2)	Training Data	Testing Data	Main Ecosystem
Svartberget (SE)	64.25, 19.77	267	1.8	614.0	93.4	2021	2022	Evergreen Needleleaf Forests
Hyltemossa (SE)	56.09, 13.41	115	7.4	707.0	110.0	2020	2021	Evergreen Needleleaf Forests
Soroe (DK)	55.48, 11.64	40	9.0	640.0	114.0	2022	2022	Deciduous Broadleaf Forests
Selhausen Juelich (DE)	50.86, 6.44	103	10.0	698.0	-	2020	2022	Croplands
Puechabon (FR)	43.74, 3.59	271	13.3	924.0	145.1	2022	2022	Evergreen Broadleaf Forests
Lamasquere (FR)	43.49, 1.23	181	13.4	677.0	157.0	2021-2022	2021-2022	Croplands
Castelporziano (IT)	41.70, 12.35	19	16.43	601.0	175.67	2021-2022	2021-2022	Mixed Forests
Voulundgaard (DK)	56.03, 9.16	67	8.1	961.0	108.0	2021-2022	2022-2023	Croplands
Gebesee (DE)	51.09, 10.91	161	9.2	534.0	119.1	2021	2022	Croplands
Lamasquere (FR)	43.49, 1.23	181	13.4	677.0	157.0	2021	2022	Croplands

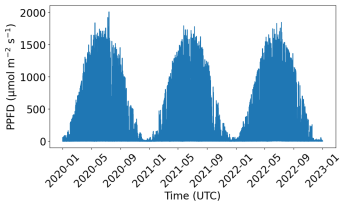

(a) Available measured PPFD data in Svartberget (SE)

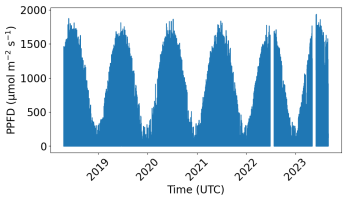

(b) Available measured PPFD data in Hyltemossa (SE)

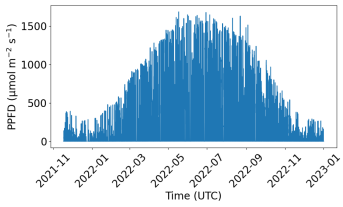

(c) Available measured PPFD data in Soroe (DK)

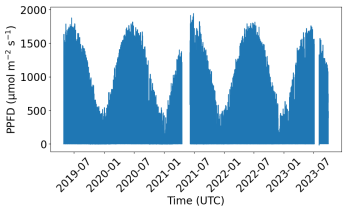

(d) Available measured PPFD data in Selhausen Juelich (DE)

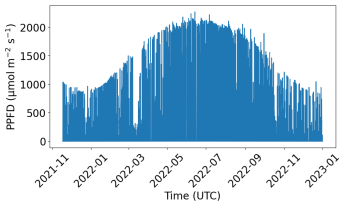

(e) Available measured PPFD data in Puechabon (FR)

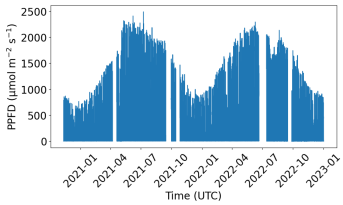

(f) Available measured PPFD data in Lamasquere (FR)

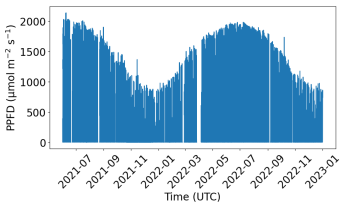

(g) Available measured PPFD data in Castelporziano2 (IT)

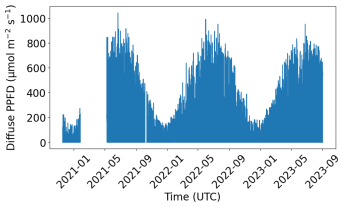

(h) Available measured diffuse PPFD data in Voulundgaard (DK)

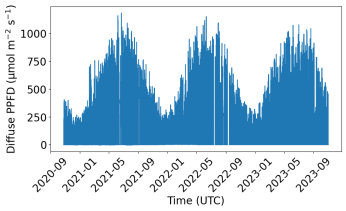

(i) Available measured diffuse PPFD data in Gebesee (DE)

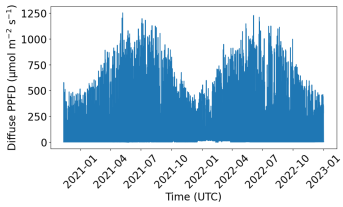

(j) Available measured diffuse PPFD data in Lamasquere (FR)

Figure 3.9: Plot of the available measured total and diffuse PPFD data in the ICOS stations selected for modeling the total and diffuse PPFD

3.5.2 Radiation data

Solar radiation data used in this work come from Photovoltaic Geographical Information System (PVGIS). PVGIS is an online tool designed to provide users with data on solar radiation and the energy production of photovoltaic (PV) systems for virtually any location in most regions of the world [35, 20]. PVGIS also provides access to hourly time series of meteorological and solar radiation variables for a Typical Meteorological Year (TMY). A typical meteorological year (TMY) comprises meteorological data with values recorded for each hour throughout a year at a specific geographical location. These data are selected from hourly observations spanning the available time period [36]. The TMY datasets generated by PVGIS follow the ISO 15927-4 procedure, as outlined by Huld et al. [21].

In this project, we utilize two distinct TMY datasets from PVGIS, corresponding to two European locations detailed in Table 3.2. These locations are Lund, situated in southern Sweden, and Seysses-Saves, located in southwestern France. The datasets provide hourly measurements of global horizontal irradiance (GHI), diffuse horizontal irradiance (DHI), and direct horizontal irradiance (DHI) that are used in this project. Visual representations of this data can be found in Figure 3.10.

Table 3.2: Comparison of solar radiation data for the locations selected for light and shade modeling: Lund (Sweden) and Seysses-Saves (France)

Location	Lund (Sweden)	Seysses-Saves (France)
Latitude, Longitude	55.71, 13.14	43.51, 1.04
Elevation	13	234
Mean An. GHI (W/m^2)	123.4	156.0
Mean An. DHI (W/m^2)	58.70	68.30
Mean An. BHI (W/m^2)	64.70	87.70

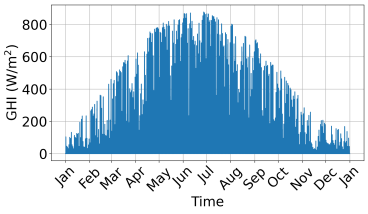

(a) Time series plot of hourly global horizontal irradiance (GHI) from TMY data for Lund (SE)

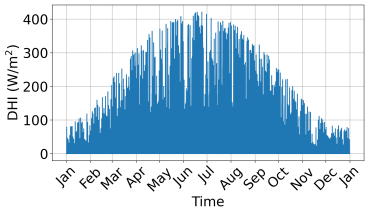

(b) Time series plot of hourly diffuse horizontal irradiance (DHI) from TMY data for Lund (SE)

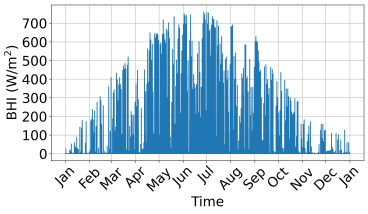

(c) Time series plot of hourly direct horizontal irradiance (BHI) from TMY data for Lund (SE)

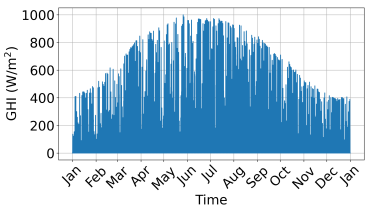

(d) Time series plot of hourly global horizontal irradiance (GHI) from TMY data for Seysses-Saves (FR)

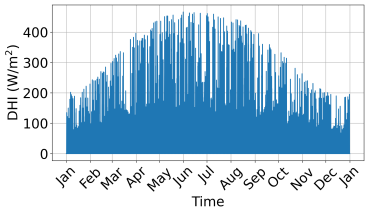

(e) Time series plot of hourly diffuse horizontal irradiance (DHI) from TMY data for Seysses-Saves (FR)

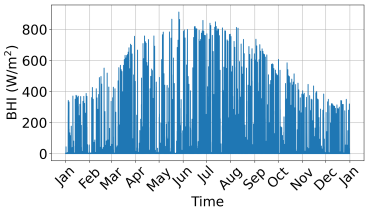

(f) Time series plot of hourly direct horizontal irradiance (BHI) from TMY data for Seysses-Saves (FR)

Figure 3.10: Time series visualization of solar irradiance measurements: DHI, GHI, and BHI from TMY Data at Lund (SE) and Seysses-Saves (FR)

Chapter 4

Result

4.1 Overview

In this chapter we present the core results of this work, building upon the theoretical framework and methodologies outlined in the previous chapters. The results are presented in a logical order for clarity. Initially, in Section 4.2 , we delve into the results from various approaches employed to estimate both total PPFD and diffuse PPFD. Subsequently, Section 4.3 is dedicated to examining the outcomes of shade and light modeling specific to single-axis tracking agrivoltaic (AV) systems. In Section 4.3, we use the findings established in Section 4.2 for estimating total PPFD and diffuse PPFD. These values are then put into Equation (2.6) to work out how much light useful for plants reaches the ground, taking into account the shadows created by the photovoltaic (PV) system over the field.

4.2 Result for estimating photosynthetic photon flux density (PPFD)

The results for estimating both total photosynthetic photon flux density (PPFD) and diffuse photosynthetic photon flux density ($PPFD_d$), across various locations in Europe, are presented in this section. The methodology for these estimations is

described in Section 3.3. The results for estimating total PPFD are presented in Section 4.2.1 and the findings for estimating PPFD_d are detailed in Section 4.2.2.

As mentioned earlier in Section 3.3.1, we assess the performance of the models for these estimations using various metrics: Mean Absolute Error (MAE), Mean Squared Error (MSE), Root Mean Squared Error (RMSE), Normalized Root Mean Squared Error (NRMSE) shown as a percentage, and R-squared (R^2). These measures help us understand how well each model predicts the values and allow us to compare their effectiveness.

4.2.1 Result for estimating total PPFD

In this section, we present the results for estimating total PPFD across seven European locations, using the three models detailed in Section 3.3:

- **Model 1:** This model is based on the formula in Equation (3.17) proposed by Foyo-Moreno et al. [14]:

  $$PPFD_{\text{total}} = a \cdot \frac{GHI}{I_0}$$

  where I_0 is the extraterrestrial radiation (Wm^{-2}) received on a plane normal to the direction of the sun and given by Equation (2.1) and GHI denotes the global horizontal irradiance (Wm^{-2}). The model uses explanatory variables, GHI and I_0 to predict total PPFD. This model employs the regression coefficient as recommended by Foyo-Moreno et al. [14], set at $a = 2681 \pm 2\,\mu\text{mol}\,\text{m}^{-2}\,\text{s}^{-1}$, to predict total PPFD. This approach provides a baseline for performance assessment.

- **Model 2:** This model employs the same formula from Foyo-Moreno et al. (Equation (3.17)) as in Model 1. The difference is that Model 2 is fine-tuned with a location-specific regression coefficient a for each selected location. This approach is designed for adaptation to local data, potentially enhancing the model's performance.

- **Model 3:** This model applies a general approach, calculating PPFD by multiplying global horizontal irradiance (GHI) with a constant factor of $2.1\,\mu\text{mol/J}$. It offers a more generalized estimation of total PPFD.

The performance results of each model in every location are presented in Table 4.1 and the corresponding bar charts of these result can be found in Figure A.8 in Appendix A. The detailed results for each location are presented in Appendix B.

Table 4.1: Comparative error metrics (MAE, MSE, RMSE, NRMSE, and R-squared) for evaluating the performance of three models in estimating PPFD across seven European locations

Station	Method	MAE	MSE	RMSE	NRMSE (%)	R^2
Svartberget (Sweden)	Model 1 ($a = 2681 \pm 2$)	17.3	1193	34.5	7.0	0.99
	Model 2 ($a = 2658 \pm 3$)	16.2	1101	33.2	6.7	0.99
	Model 3	35.7	2941	54.2	10.9	0.98
Hyltemossa (Sweden)	Model 1 ($a = 2681 \pm 2$)	73.7	11561	107.5	24.2	0.94
	Model 2 ($a = 2267 \pm 2$)	18.4	665	25.8	5.8	1.00
	Model 3	100.2	20459	143.0	32.1	0.89
Soroe (Denmark)	Model 1 ($a = 2681 \pm 2$)	104.0	15873	126.0	19.0	0.90
	Model 2 ($a = 2313 \pm 3$)	21.7	872	29.5	4.4	0.99
	Model 3	145.0	29376	171.4	25.8	0.81
Selhausen Juelich (Germany)	Model 1 ($a = 2681 \pm 2$)	40.2	3379	58.1	10.0	0.98
	Model 2 ($a = 2500 \pm 2$)	16.1	588	24.3	4.2	1.00
	Model 3	69.9	9087	95.3	16.5	0.96
Lamasquere (France)	Model 1 ($a = 2681 \pm 2$)	76.1	9653	98.2	13.4	0.97
	Model 2 ($a = 2864 \pm 6$)	52.7	6141	78.4	10.7	0.98
	Model 3	57.0	6561	81.0	11.0	0.98
Puechabon (France)	Model 1 ($a = 2681 \pm 2$)	77.0	8427	91.8	12.0	0.98
	Model 2 ($a = 2913 \pm 4$)	37.2	2474	49.7	6.5	0.99
	Model 3	41.0	2965	54.5	7.1	0.99
Castelporziano2 (Italy)	Model 1 ($a = 2681 \pm 2$)	113.0	18695	137	18.0	0.94
	Model 2 ($a = 3066 \pm 5$)	44.5	4791	69.2	9.1	0.99
	Model 3	78.9	10299	101.5	13.3	0.97

4.2.1.1 Summary of the results

In all the locations, Model 2 either outperforms the others or is among the top-performing models. When comparing Models 1 and 3, Model 1 exhibits better performance in four out of the seven locations: Svartberget, Hyltemossa, Soroe, and Selhausen Juelich. While, Model 3 outperforms Model 1 in three locations: Puechabon, Lamasquere, and Castelporziano2.

Moreover, Models 1 and 3 tend to predominantly overestimate the measured PPFD values in four locations: Svartberget, Hyltemossa, Soroe, and Selhausen Juelich, while they mostly underestimate the values in Puechabon and Castelporziano2.

4.2.2 Result for estimating diffuse PPFD

In this section, we present the results for estimating diffuse PPFD in three locations across Europe, using the three models detailed in Section 3.3:

- **Model A:** This model is based on the formula in Equation (3.17) proposed by Foyo-Moreno et al. [13]:

  $$PPFD_{\mathrm{d}} = a \cdot \frac{DHI}{I_0}$$

  where I_0 is the extraterrestrial radiation (Wm^{-2}) received on a plane normal to the direction of the sun and given by Equation (2.1) and DHI denotes the diffuse horizontal irradiance (Wm^{-2}). The model uses explanatory variables, DHI and I_0 to predict diffuse PPFD.

  This model adopts the regression coefficient as proposed by Foyo-Moreno et al. [13], set at $a = 2681 \pm 2\,\mu\mathrm{mol\,m^{-2}\,s^{-1}}$.

- **Model B:** This model employs the same formula from Foyo-Moreno et al. (Equation (3.17)) as in Model A. The difference is that this model is fine-tuned with a location-specific regression coefficient a for each selected location. This approach is intended to adjust the model to local data, potentially leading to improved performance.

- **Model C:** This model applies a general approach, calculating PPFD by multiplying global diffuse horizontal irradiance (DHI) with a constant factor of $2.1\,\mu$mol/J. It offers a more generalized estimation of diffuse PPFD.

The performance results of each model for estimating diffuse PPFD in every location are detailed in Table 4.2. Corresponding bar charts illustrating these results are provided in Figure A.12 in Appendix A, while the detailed results for each location are available in Appendix B.

Table 4.2: Comparative error metrics (MAE, MSE, RMSE, NRMSE, and R-squared) for evaluating the performance of three models in estimating diffuse PPFD across three European locations

Station	Method	MAE	MSE	RMSE	NRMSE (%)	R^2
Voulundgaard (Denmark)	Model A ($a = 2681 \pm 2$)	38.1	2596	50.9	20.8	0.91
	Model B ($a = 2423 \pm 7$)	28.6	1826	43.0	17.4	0.94
	Model C	46.9	3819	61.8	25.2	0.87
Gebesee (Germany)	Model A ($a = 2681 \pm 2$)	38.9	3236	56.9	20.4	0.92
	Model B ($a = 2814 \pm 8$)	37.0	2734	52.3	18.7	0.93
	Model C	37.6	2730	52.2	18.7	0.93
Lamasquere (France)	Model A ($a = 2681 \pm 2$)	52.0	5267	72.6	22.7	0.89
	Model B ($a = 2874 \pm 10$)	48.7	4309	65.6	20.5	0.91
	Model C	50.0	4555	67.5	21.1	0.90

4.2.2.1 Summary of the results

Among the three models used for estimating diffuse PPFD, Model B, with location specific coefficient, showed better results compared to Models A and C in Voulundgaard and Lamasquere. In Gebesse, the performance of Models B and C was very similar.

However, the tendencies observed for estimating diffuse PPFD are not as clear as those for total PPFD estimation (discussed in Section 4.2.1). While Models A and C seem to mostly overestimate diffuse PPFD values in Voulundgaard and underestimate them in Lamasquere and Gebesse, these tendencies are less pronounced (see Appendix B).

4.3 Result for shade and light modeling

This section begins by presenting the specifications of the AV systems used for shading simulations in Section 4.3.1. After that we present the result for estimating total and diffuse PPFD in the two locations, presented in Table 3.2, selected for our shade and light model simulations in Section 4.3.2. we continue by presenting the calculated hourly shading factors in Section 4.3.3 for the selected configurations and the two locations outlined in Table 3.2. Following this, Section 4.3.4 presents a comparison of the PPFD values at ground level in the selected AV system configurations and in two different locations. Lastly, Section Section 4.3.5 focuses on the PPFD distribution within the discretised area between the rows for the selected configurations and locations.

4.3.1 Geometric design parameters for one-axis tracker AV systems

To simulate shading scenarios, two distinct configurations of AV systems were investigated. The details of these configurations are provided in Table 4.3. The results are presented for these two configurations placed in two locations specified in Table 3.2.

Model Design Parameters	Configuration C1	Configuration C2
Row length (m)	20	20
Row width (m)	2.5	5.0
Row height (m)	1.5	3.0
Number of rows	2	2
Row spacing (Pitch) (m)	10	10
Tracker	Single axis	Single axis
Backtracking	True	True
Maximum tracker rotation angle (°)	55	55
Tracker axis azimuth angle (°)	0	0
Tracker axis elevation angle (°)	0	0

Table 4.3: Design parameters specifying two configurations of one-axis tracker PV system. Configuration C1 and Configuration C2 represent distinct sets of parameters used for evaluating the effects of shading and light distribution in an AV system.

4.3.2 Estimation of total and diffuse PPFD using locally adapted coefficients

To apply Equation 2.6 in calculating the total PPFD that a surface receives after considering shading effects, it is essential to initially estimate both the total and diffuse PPFD. These estimates are based on TMY radiation data, including GHI and DHI measurements, for the two locations specified in Table 3.2.

To estimate the total and diffuse PPFD for the locations specified in Table 3.2, we utilized the findings from Section 4.2. The results indicated that the models in Equation (3.17), for estimating total and diffuse PPFD, were most effective when using a locally adapted coefficient a, derived by fitting the model to local data. Therefore, for our total PPFD and diffuse PPFD estimates, we applied coefficients from the nearest ICOS station, in terms of latitude, to our chosen locations for shading simulations.

Specifically, for the total PPFD estimation using the model in Equation (3.17), we employed the coefficient determined at Soroe (DK) for Lund (SE) and the coefficient from Lamasquere (FR) for Seysses-Saves (FR). These locally adapted coefficients are listed in Table 4.1.

For the diffue PPFD estimation using the model in Equation (3.17) we used the

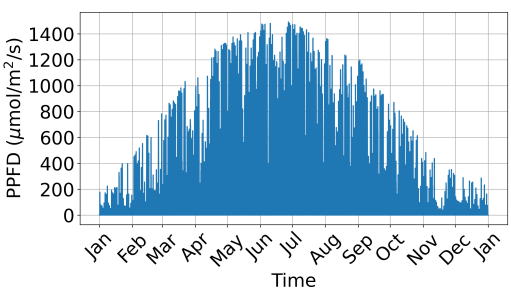

(a) Estimated diffuse PPFD for Lund (SE)

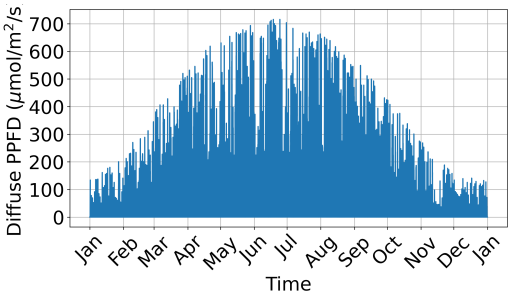

(b) Estimated diffuse PPFD for Lund (SE)

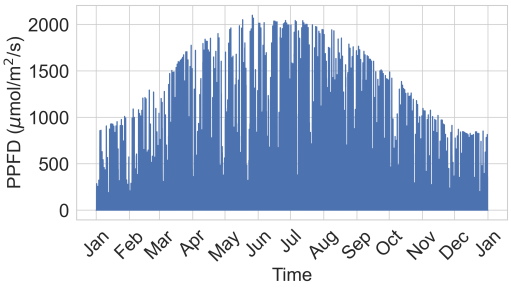

(c) Estimated total PPFD for Seysses-Saves (FR)

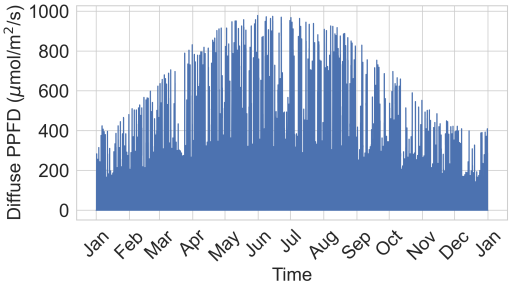

(d) Estimated diffuse PPFD for Seysses-Saves (FR)

Figure 4.1: Plots of estimated hourly values of total PPFD and diffuse PPFD for Lund (SE) and Seysses-Saves (FR)

coefficient obtained at Voulundgaard (DK) for Lund (SE) and the coefficient from Lamasquere (FR) for Seysses-Saves (FR). These locally fitted coefficients are presented in Table 4.2.

4.3.3 Shading factors in AV systems

In this section, we focus on the ground level area located between the rows of PV solar panels, as depicted in Figure 3.3. This reference area is defined by a width equal to the pitch of the rows and a length corresponding to the rows' length. This area serves as the reference area for all subsequent calculations.

The calculations for hourly direct and diffuse shading factors were carried out for two configurations outlined in Table 4.3 and for both locations specified in Table 3.2. The results were hourly time series of direct and diffuse shading factors spanning

an entire year. From these results, data for four representative days were selected and are presented in Figure 4.2 for direct shading factors and Figure 4.3 for diffuse shading factors. Figure 4.2a shows the direct shading factors for configuration C1 in Lund. The pattern indicates similar amount of shading during the summer solstice and spring and autumn equinoxes, although the values are slightly higher during summer solstice. These values are higher compared to shading during the winter solstice. Figure 4.2b illustrates the direct shading factors for configuration C2 in Lund. Similar to C1, C2 experiences the most shading on the summer solstice and the least during the winter solstice. However, the extent of shading appears to be higher in C2 compared to C1. The exception is the winter solstice where the values corresponding to configuration C1 are slightly higher compared to values for configuration C2.

Figure 4.2c, depicting the direct shading factors for configuration C1 in Seysses-Saves, exhibits patterns similar to those observed for the same configuration in Lund. Notably, the direct shading factors during the winter solstice in Seysses-Saves are higher in comparison to those in Lund. Figure 4.2d for configuration C2 in Seysses-Saves also shows similar results to those obtained for the same configuration in Lund but with a noticeable increase in the shading factor during the winter solstice.

Examining the midday hours of the days shows that the values for direct shading factors for configuration C2 are higher than those for configuration C1. This trend occurs in both locations during the summer solstice, and the spring and autumn equinoxes. This trend also holds for the winter solstice in Seysses-Saves.

Figure 4.3 presents time series plots of hourly diffuse shading factors for four representative days, corresponding to the two configurations described in Table 4.3 and observed in both Lund and Seysses-Saves. It is important to note that the diffuse shading factor is influenced by the geometry of the receiver surface and obstructions, and not by the sun's position. As a result, the diffuse shading factors calculated for each configuration display similar values across both locations during the day. For configuration C1, the diffuse shading factors range from approximately 20 to 25% for all chosen days, whereas for configuration C2, they are between 32 to 42% in both locations. This indicates that configuration C2 experiences more shading in terms of diffuse radiation compared to C1.

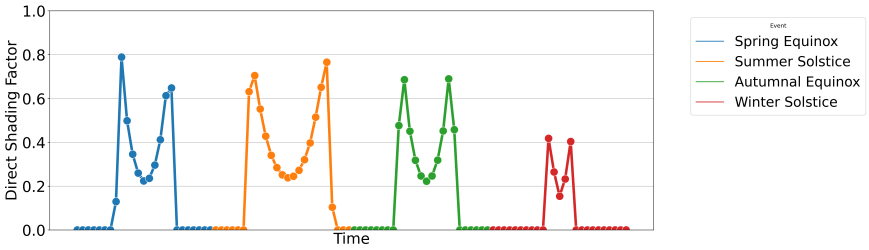

(a) Hourly direct shading factors across four representative days for configuration C1 in Lund (SE)

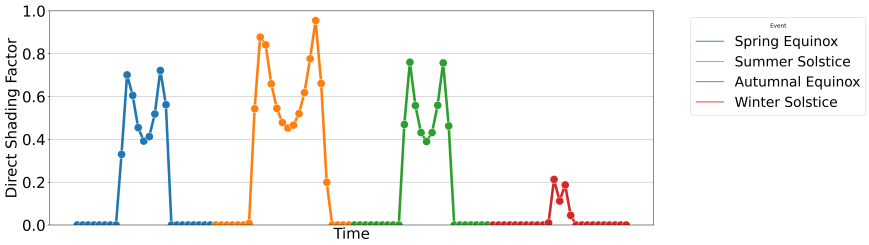

(b) Hourly direct shading factors across four representative days for configuration C2 in Lund (SE)

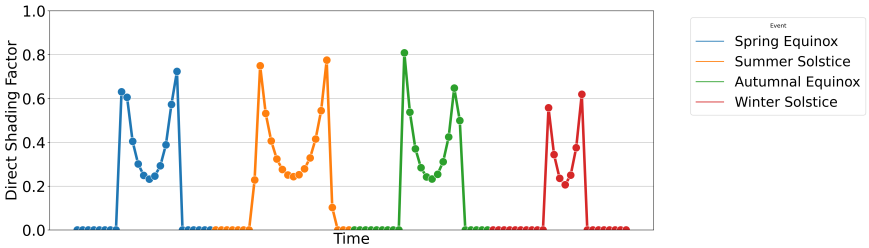

(c) Hourly direct shading factors across four representative days for configuration C1 in Seysses-Saves (FR)

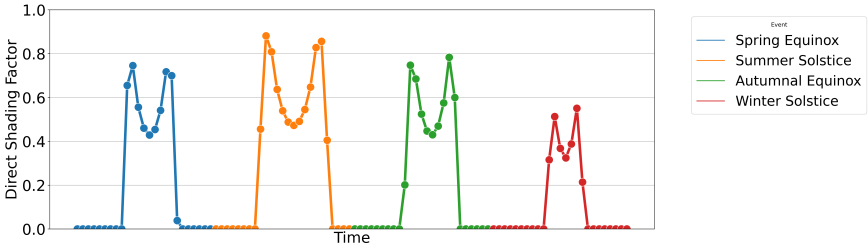

(d) Hourly direct shading factors across four representative days for configuration C2 in Seysses-Saves (FR)

Figure 4.2: Time series of hourly direct shading factors for configurations C1 and C2 across representative days in Lund (SE) and Seysses-Saves (FR)

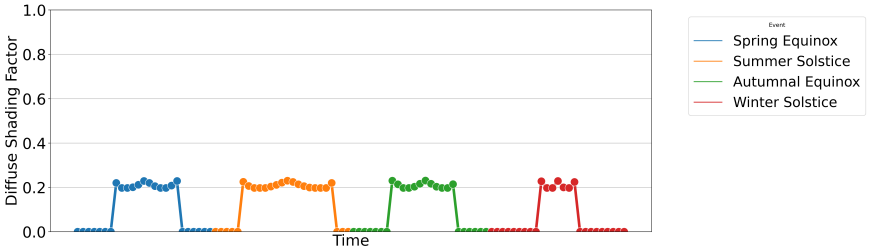

(a) Hourly diffuse shading factors across four representative days for configuration C1 in Lund (SE)

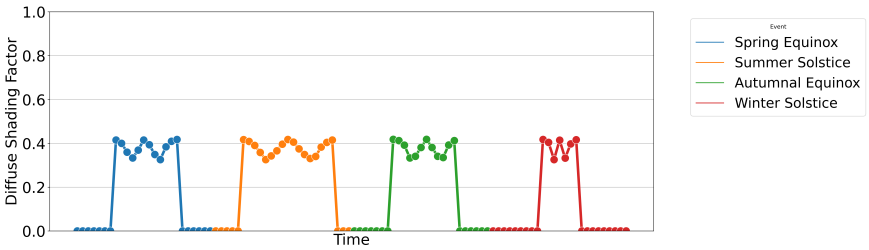

(b) Hourly diffuse shading factors across four representative days for configuration C2 in Lund (SE)

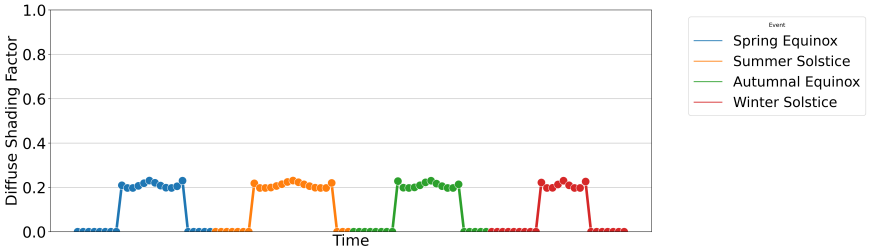

(c) Hourly diffuse shading factors across four representative days for configuration C1 in Seysses-Saves (FR)

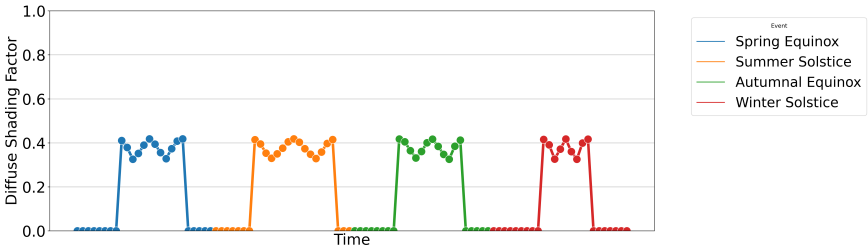

(d) Hourly diffuse shading factors across four representative days for configuration C2 in Seysses-Saves (FR)

Figure 4.3: Hourly time series of diffuse shading factors for configurations C1 and C2 for four representative days in Lund (SE) and Seysses-Saves (FR)

4.3.4 Reduction in PPFD in AV systems

In this section, our attention is again centered on the area at ground level situated between the rows of PV solar panels, as illustrated in Figure 3.3. The area under consideration is characterized by its width, which matches the pitch of the rows, and its length, which is equivalent to that of the rows themselves.

Table 4.4 presents the total yearly reduction in PPFD values for the two AV system configurations detailed in Table 4.3 for locations in Lund, Sweden, and Seysses-Saves, France. The results shows that in both locations the highest yearly reduction in total PPFD is associated with configuration C2. This result is consistent with what was observed in the computed shading factors in Section 4.3.3 where the highest levels of shading factors were observed in connection with configuration C2. Additionally, the amount of PPFD reduction is almost the same for each system type in both locations.

Figure 4.4 presents a comparison of the variations in monthly averages of daily sums of hourly PPFD values for Lund, Sweden, and Seysses-Saves, France. These comparisons include 95% confidence intervals and contrast the scenarios with and without the AV system for configurations C1 and C2. The plots illustrate a significantly greater decrease in the monthly average PPFD values associated with configuration C2 compared to C1 in both locations.

Table 4.4: Annual reduction in photosynthetic photon flux density (PPFD) for two AV system configurations in Lund, Sweden, and Seysses-Saves, France

Location	**Configuration C1**	**Configuration C2**
Lund (SE)	30.0%	54.3%
Seysses-Saves (FR)	29.0%	54.4%

4.3.5 PPFD distribution in AV systems

To gain a better understanding of how PPFD is distributed at ground level in AV systems, we shift our attention from the entire reference area between the rows of PV panels, as depicted in Figure 3.3, to a more detailed, discretised examination of this area. The area between the rows is divided into 1 m $\times$ 1 m cells and shading factors are calculated for each individual segment.

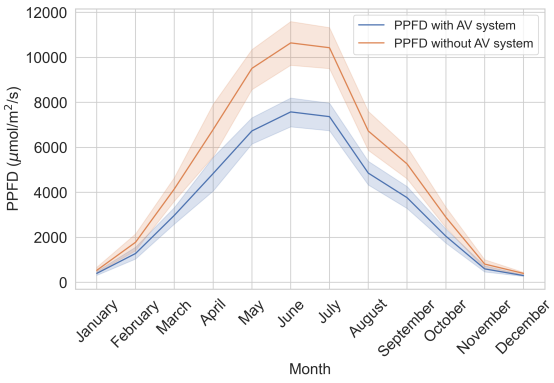

(a) Variation in monthly averages of daily sums of PPFD, with 95% CI, with and without the AV system with configuration C1 in Lund.

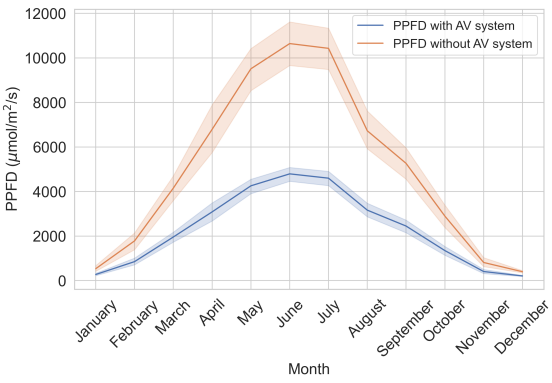

(b) Variation in monthly averages of daily sums of PPFD, with 95% CI, with and without the AV system with configuration C2 in Lund.

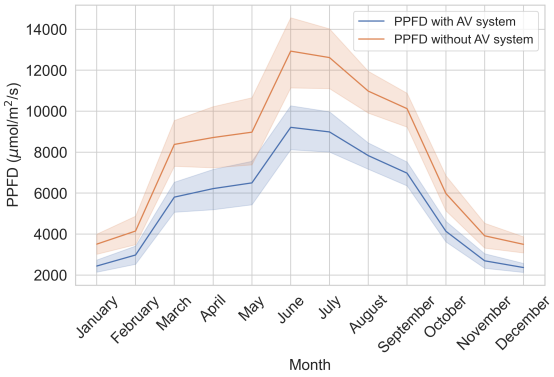

(c) Variation in monthly averages of daily sums of PPFD, with 95% CI, with and without the AV system with configuration C1 in Seysses-Saves.

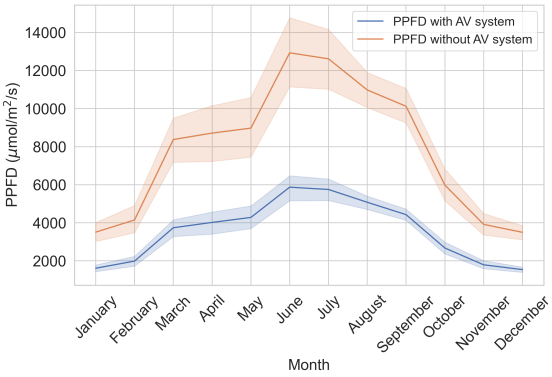

(d) Variation in monthly averages of daily sums of PPFD, with 95% CI, with and without the AV systwm with configuration C2 in Seysses-Saves.

Figure 4.4: Comparison of the ground-level monthly average of daily summations of PPFD with 95% confidence intervals (CI) in two locations, Lund and Seysses-Saves, each with configurations C1 and C2, highlighting the effects of implementing an AV system.

Figure 4.5 shows the total yearly PPFD distribution for the two AV configurations detailed in Table 4.3 in Lund, Sweden and Seysses-Saves, France. Table 4.5 presents the yearly light homogeneity index (LHI) (see Section 3.4) calculated from the total yearly PPFD values for each configuration in Lund and Seysses-Saves. The results indicate that light distribution is slightly more homogeneous, on the ground area between the rows of PV panels, in configuration C1 compared to C2 in both locations.

The total yearly reduction of PPFD in the different sections of the discretised area between the rows is presented in Figure 4.6. The figure includes this result for the two configurations C1 and C2 in two locations, Lund and Seysses-Saves.

The plots in Figure 4.6 display the annual PPFD reduction calculated for each individual segment within the discretised area between the rows of PV panels. This includes results for configurations C1 and C2 in both Lund and Seysses-Saves. The results indicate that configuration C2 results in a greater decrease in PPFD across all sections of the discretized ground-level area between the rows, compared to C1 in both locations. Specifically, the total annual PPFD reduction ranges from about 5 to 65% for configuration C1 in both places, and from 10 to 75% for configuration C2.

Table 4.5: Annual light homogeneity index (LHI) for two AV system configurations C1 and C2 in Lund, Sweden, and Seysses-Saves, France

Location	**Configuration C1**	**Configuration C2**
Lund (SE)	74.6%	71.4%
Seysses-Saves (FR)	72.4%	69.1%

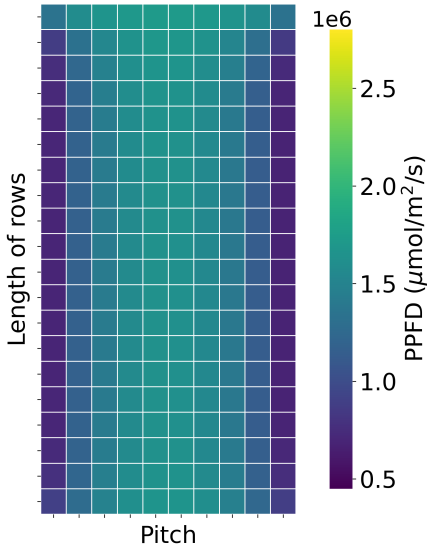

(a) Total annual distribution of PPFD at ground level for AV system configuration C1 in Lund (SE)

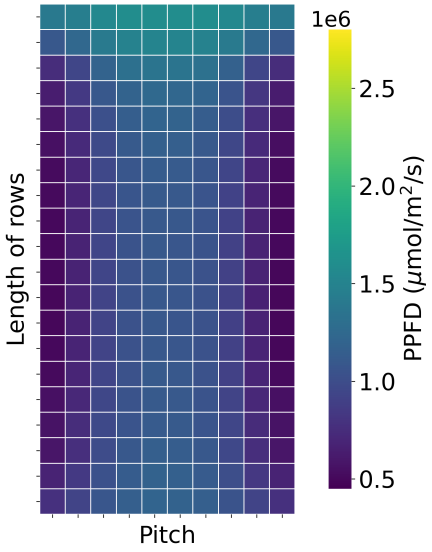

(b) Total annual distribution of PPFD at ground level for AV system configuration C2 in Lund (SE)

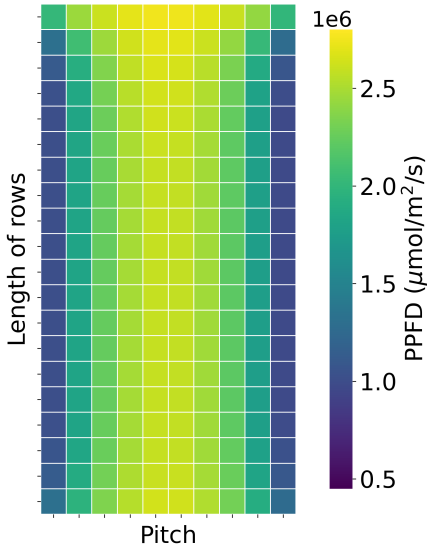

(c) Total annual distribution of PPFD at ground level for AV system configuration C1 in Seysses-Saves (FR)

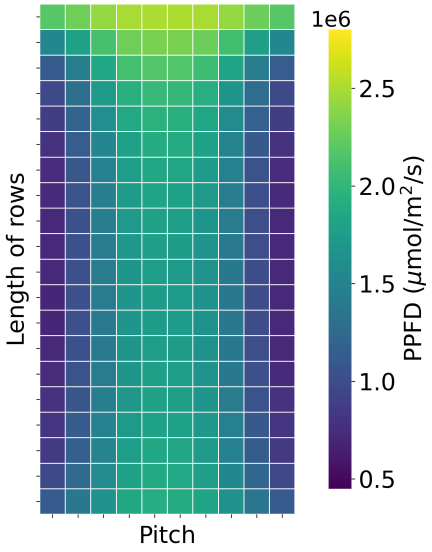

(d) Total annual distribution of PPFD at ground level for AV system configuration C2 in Seysses-Saves (FR)

Figure 4.5: Comparison of total annual distribution of PPFD at ground level for AV system configurations C1 and C2 in Lund (SE) and Seysses-Saves (FR)

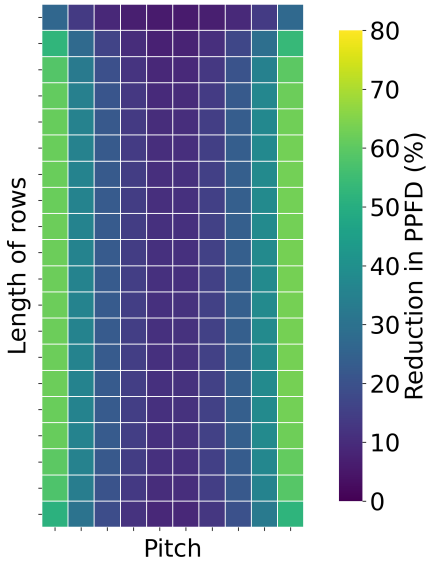

(a) Total annual reduction in PPFD at ground level for AV system configuration C1 in Lund (SE)

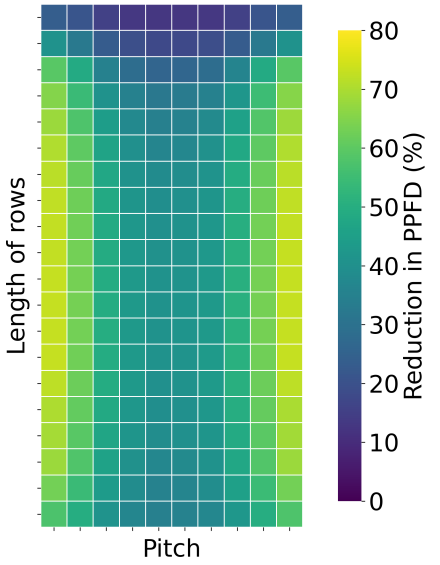

(b) Total annual reduction in PPFD at ground level for AV system configuration C2 in Lund (SE)

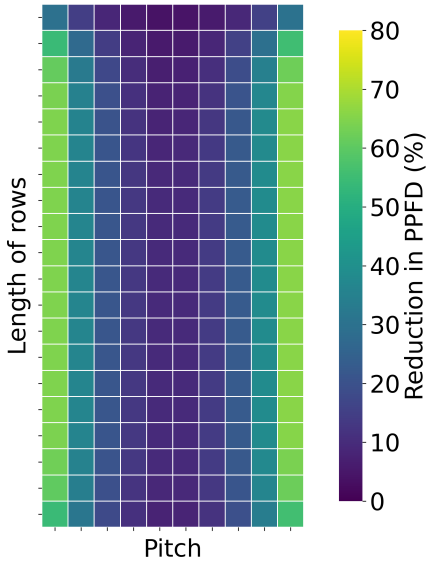

(c) Total annual reduction in PPFD at ground level for AV system configuration C1 in Seysses-Saves (FR)

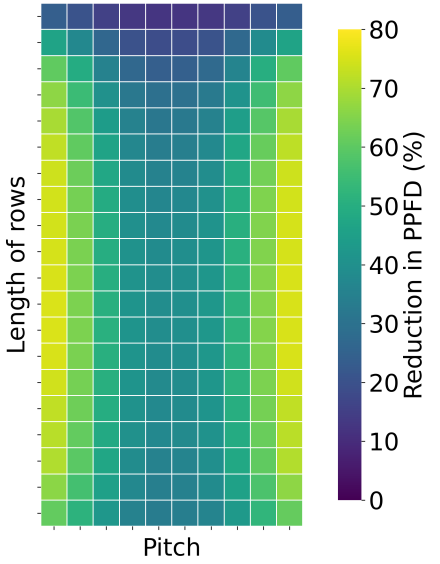

(d) Total annual reduction in PPFD at ground level for AV system configuration C2 in Seysses-Saves (FR)

Figure 4.6: Comparison of total annual reduction of PPFD at ground level for AV system configurations C1 and C2 in Lund (SE) and Seysses-Saves (FR)

Chapter 5

Discussion & future work

5.1 Development and aassessment of a simulation model for light and shade in AV systems

In this project, our primary objective was to construct a simulation model designed for the analysis of light and shading within AV settings, focusing particularly on PV systems with horizontal single-axis tracking. Our approach involved the estimation of radiation in the photosynthetically active wavelength range, based on GHI and DHI data. This approach made it possible to do an assessment of available radiation relevant for plant growth in AV systems. Since crop relevant light measurements are not available for all potential AV sites, this was an important part of the process. The model's strength lies in its ability to simulate shadows cast by the PV system on the field and to map the distribution of light at ground level, making it a useful tool for optimizing AV system configurations for agricultural productivity.

In addition, the ability of our methodology to adapt to different types of AV systems, including those with fixed tilt or two-axis trackers, shows its wide range of application potentials.

5.1.1 Impact of AV system configuration vs. geographic location on PPFD distribution & light homogeneity

The model allows for a comprehensive analysis of the impact of system configuration and geographic location on PPFD distribution and light homogeneity between the rows, as detailed in the following results.

The results illustrated in Figure 4.6 indicate that in the two selected locations, the extent and pattern of yearly reduction in PPFD across the descretised area between the panels are mainly determined by the configuration of the AV system, rather than by the specific geographic locations. This observation is further supported by the results in Table 4.4, which shows that the same AV system configuration leads to nearly identical percentages of PPFD reduction in both locations.

The yearly amount of PPFD received in each cell is influenced by both the geographic location and the configuration of the system as clearly shown in Figure 4.5. This appears to be primarily due to the differences in the total amount of radiation available annually at each location.

The result in Table 4.5 shows that the uniformity of yearly light distribution in the segmented area between rows of panels for the same AV system configuration is quite similar in the selected locations. The LHI values appear to be mainly determined by the type of configuration rather than the geographical location. This is indicated by the very close LHI values obtained for the same configurations.

However, it is important to be cautious about generalizing these findings. A more comprehensive comparison and analysis, involving a diverse range of locations, is necessary to confirm if these trends are persistent.

Furthermore, the AV systems examined in Section 4.3 were limited to configurations with just two rows of PV panels, and hence, excluding the potential shading effect from multiple rows. Adding more rows of PV panels to the AV system can be beneficial for the analysis of the shading scenarios by bringing it closer to the real-world settings. This addition could help us better understand how the presence of multiple rows affect the amount and distribution of PPFD, received in the areas placed in the middle of these rows.

Figure 4.5 shows a variation in the PPFD that reaches different parts of the analyzed area. Specifically, the amount of PPFD at the edges near the ends of the rows differs

from that in the central section. In our model, the length of the analyzed area is currently equal to that of the PV panel rows. To address the edge effect, it might be useful to modify the model. One approach could be to extend the length of the PV panel rows while keeping the current length of the analyzed area. Comparing the results of this adjusted model with the existing one could provide valuable insights into the impact of the edge effect on both the homogeneity of distribution of PPFD and the total PPFD received on the ground area over a given time period.

5.1.2 Model verification

It is important to recognize the limitations of this project. The verification of calculated shading factors was not within the scope and resources of this work, and therefore, the precision of these values remains an area for future work. This could be done using tools like PVsyst [37] or through the collection and analysis of empirical data.

5.2 PPFD estimation

The performance and accuracy of the models used to estimate total PPFD improved significantly when locally fitted coefficient was applied in the regression model. Therefore, for optimal estimation in various locations, access to local PPFD data is beneficial. Using a general coefficient might lead to less accurate results, as indicated by the results in Table 4.1. The locally fitted regression coefficients in this table table suggest a trend where the ratio of total PPFD to GHI tends to increase as the latitude decreases. However, an anomaly was observed in Svartberget (SE), showing a higher PPFD to GHI ratio than expected based on this trend. To confirm this trend's validity, it is necessary to analyze data from a wider range of locations. Employing a more general method for estimating total PPFD from GHI measurements, based on these ratios, could offer a more practical approach. However, this trend was not evident in the ratio between diffuse PPFD and DHI (see Table 4.2), but it is worth noting that our data for estimating diffuse PPFD was limited to just three locations in Europe.

Appendix A

Bar charts of the performance results of three models for estimating total and diffuse PPFD in various locations

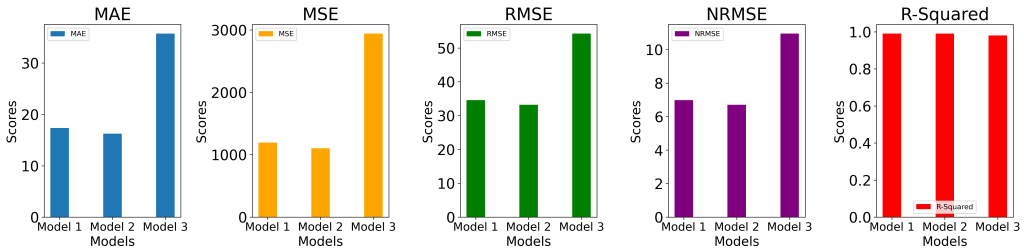

Figure A.1: Comparison of the statistical results for performance of three models in Svartberget (SE)

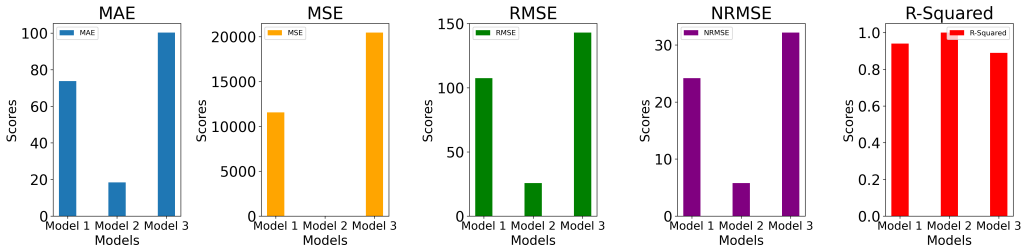

Figure A.2: Comparison of the statistical results for performance of three models in Hyltemossa (SE)

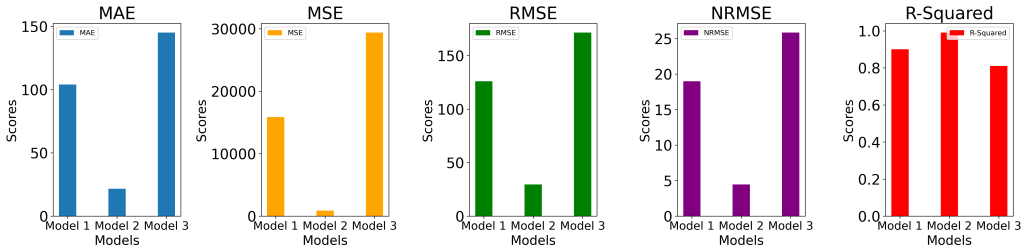

Figure A.3: Comparison of the statistical results for performance of three models in Soroe (DK)

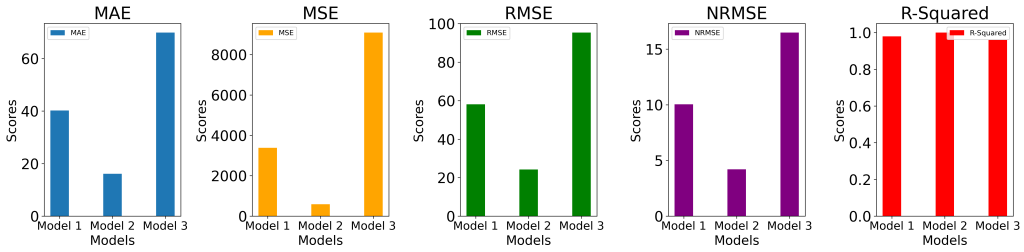

Figure A.4: Comparison of the statistical results for performance of three models in Selhausen Juelich (DE)

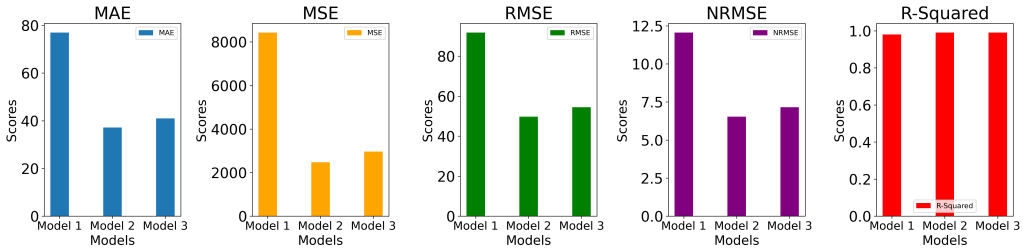

Figure A.5: Comparison of the statistical results for performance of three models in Puechabon (FR)

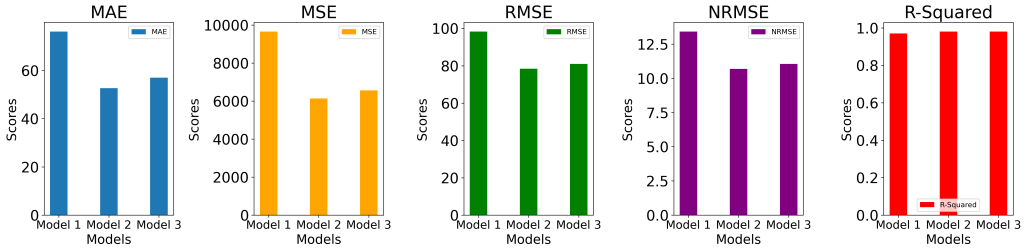

Figure A.6: Comparison of the statistical results for performance of three models in Lamasquere (FR)

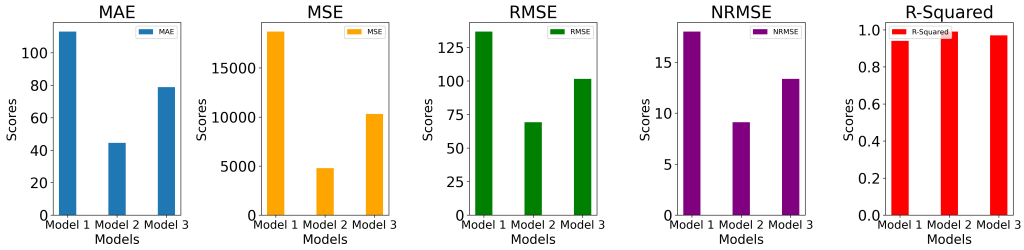

Figure A.7: Comparison of the statistical results for performance of three models in Castelporziano2 (IT)

Figure A.8: The performance results of three models for estimating total PPFD in seven locations in Europe, in terms of MAE (mean absolute erro), MSE (mean squared error), RMSE (root mean squared error), NRMSE (normalized root mean squared error) and R-squared

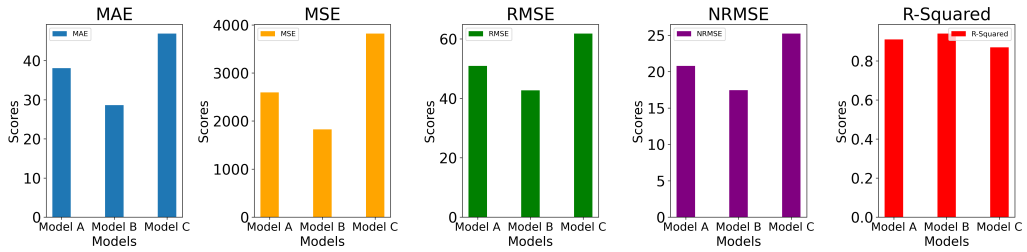

Figure A.9: Comparison of the statistical results for performance of three models in Voulundgaard (DK)

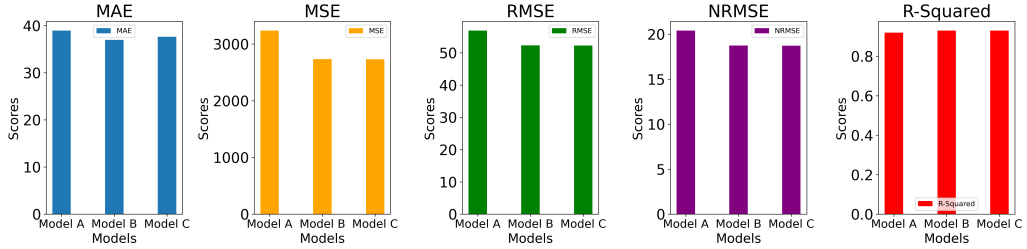

Figure A.10: Comparison of the statistical results for performance of three models in Gebesee (DE)

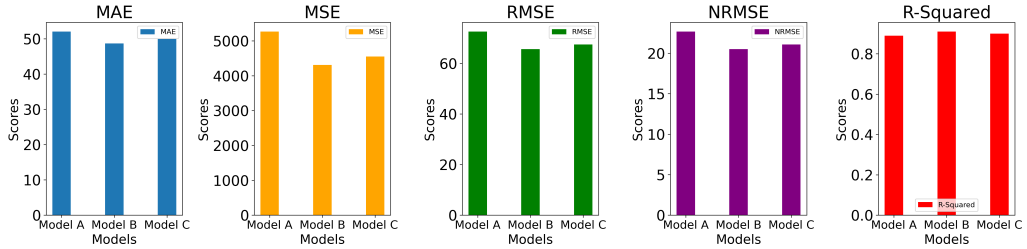

Figure A.11: Comparison of the statistical results for performance of three models in Lamasquere (FR)

Figure A.12: The performance results of three models for estimating diffuse PPFD in three locations in Europe, in terms of MAE (mean absolute erro), MSE (mean squared error), RMSE (root mean squared error), NRMSE (normalized root mean squared error) and R-squared

Appendix B

Results of total and diffuse PPFD estimation in various locations

The results for estimating both total and diffuse PPFD, in each chosen, location are presented. It should be noted that in the plots displayed here, the term 'error' denotes the difference between the estimated PPFD, or diffuse PPFD, from each model and the respective actual measured PPFD values.

B.1 Result for estimating total PPFD in seven location across Europe

B.1.1 Svartberget (SE)

Figure B.1 presents both scatter plots and histograms of the estimation errors for three different PPFD estimation models applied to the Svartberget testing dataset. Additionally, Table 4.1 contains the statistical result for estimating total PPFD in Svartberg using the three approaches. Based on both the statistical results in Table 4.1 and the visual representations in Figure B.1, Model 2 is the best performing model amongst the three models. While Models 1 and 2 demonstrate similar overall performance, Model 3 shows a tendency to overestimate PPFD values.

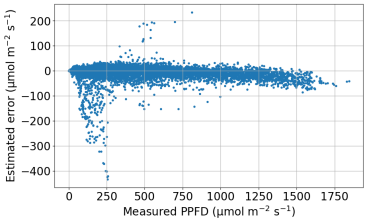

(a) Scatter plot depicting the estimation errors versus the measured PPFD values for Model 1.

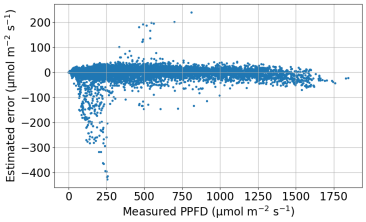

(b) Scatter plot depicting the estimation errors versus the measured PPFD values for Model 2.

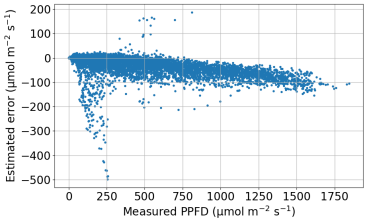

(c) Scatter plot depicting the estimation errors versus the measured PPFD values for Model 2.

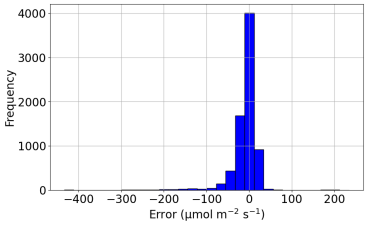

(d) Histogram of the estimation errors for Model 1.

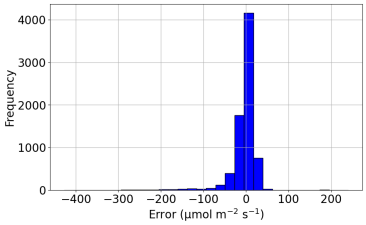

(e) Histogram of the estimation errors for Model 2.

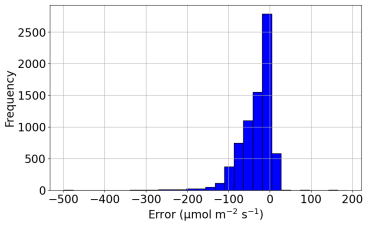

(f) Histogram of the estimation errors for Model 3.

Figure B.1: Histograms and scatterplots illustrating the estimation errors of the three distinct models for Svartberget (SE)

B.1.2 Hyltemossa (SE)

Figure B.2 shows both scatter plots and histograms of the estimation errors for three different PPFD estimation models applied to the Hyltemossa testing dataset. Additionally, Table 4.1 provides the statistical results for estimating total PPFD in Hyltemossa using the three models. An examination of both the statistical result in Table 4.1 and the estimation errors in Figure B.2 suggest among the three, Model 2 is observed to have the best performance. The results also show that both Models 1 and 3 tend to consistently predict higher PPFD values compared to the actual measurements. However, Model 1 demonstrates better performance compared to Model 3.

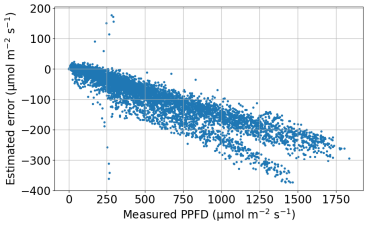

(a) Scatter plot depicting the estimation errors versus the measured PPFD values for Model 1.

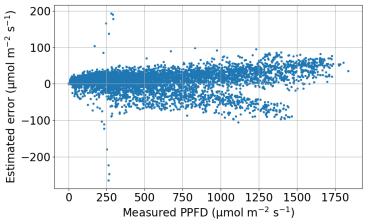

(b) Scatter plot depicting the estimation errors versus the measured PPFD values for Model 2.

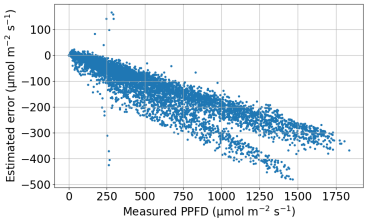

(c) Scatter plot depicting the estimation errors versus the measured PPFD values for Model 3.

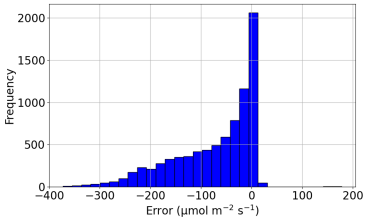

(d) Histogram of the estimation errors for Model 1.

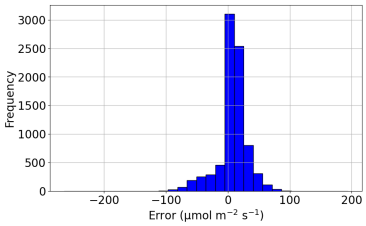

(e) Histogram of the estimation errors for Model 2.

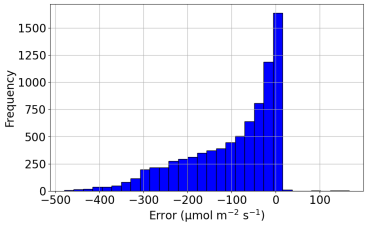

(f) Histogram of the estimation errors for Model 3.

Figure B.2: Histograms and scatterplots illustrating the estimation errors of the three distinct models for Hyltemossa (SE)

B.1.3 Soroe (DK)

Figure B.3 shows scatter plots and histograms illustrating the estimation errors of three distinct PPFD estimation models when applied to the Soroe test dataset. In addition, Table 4.1 details the statistical result of total PPFD estimation in Soroe using these three methods. A review of both the statistical result in Table 4.1 and the estimation errors in Figure B.3 suggest that Model 2 is the most effective model among the three models. While Models 1 and 3 tend to overestimate PPFD values in comparison to actual measurements, Model 1 is observed to have a better performance compared to Model 3.

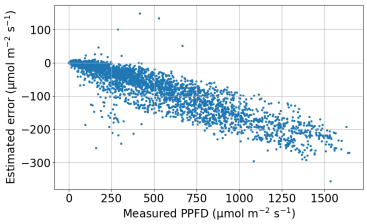

(a) Scatter plot depicting the estimation errors versus the measured PPFD values for Model 1.

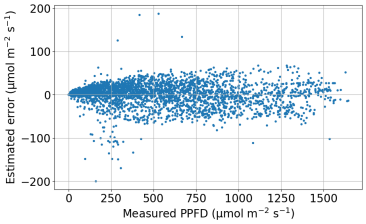

(b) Scatter plot depicting the estimation errors versus the measured PPFD values for Model 2.

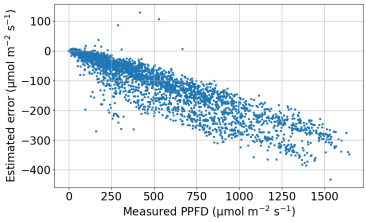

(c) Scatter plot depicting the estimation errors versus the measured PPFD values for Model 3.

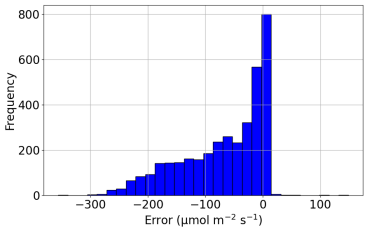

(d) Histogram of the estimation errors for Model 1.

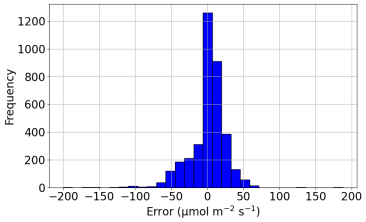

(e) Histogram of the estimation errors for Model 2.

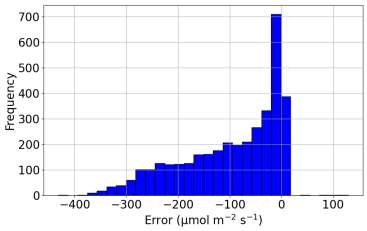

(f) Histogram of the estimation errors for Model 3.

Figure B.3: Histograms and scatterplots illustrating the estimated errors of the three distinct models for Soroe (DK)

B.1.4 Selhausen Juelich (DE)

Figure B.4 shows scatter plots and histograms of the estimation errors for three unique PPFD estimation models applied to the Selhausen Juelich testing dataset. Additionally, Table 4.1 presents the statistical result of total PPFD estimation in Soroe utilizing these models. An examination of the statistical results in Table 4.1 and the visual insights from Figure B.3 indicates Model 2 is the best performing model. While Models 1 and 3 appear to almost consistently predict higher PPFD values than the actual measurements, Model 1 shows better result compared to Model 3.

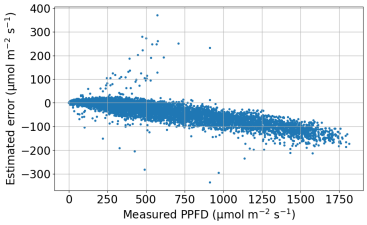

(a) Scatter plot depicting the estimation errors versus the measured PPFD values for Model 1.

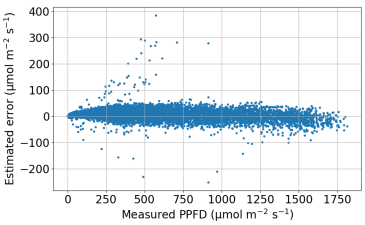

(b) Scatter plot depicting the estimation errors versus the measured PPFD values for Model 2.

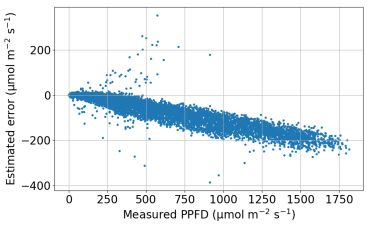

(c) Scatter plot depicting the estimation errors versus the measured PPFD values for Model 3.

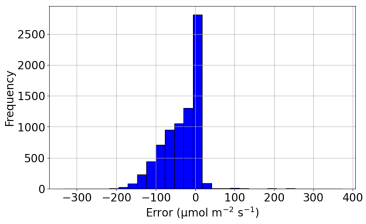

(d) Histogram of the estimation errors for Model 1.

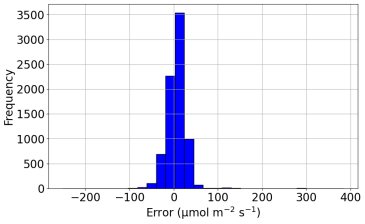

(e) Histogram of the estimation errors for Model 2.

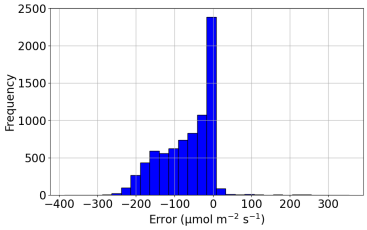

(f) Histogram of the estimation errors for Model 3.

Figure B.4: Histograms and scatterplots illustrating the estimated errors of the three distinct models for Selhausen Juelich (DE)

B.1.5 Puechabon (FR)

Figure B.5 displays scatter plots and histograms of the estimation errors for three unique PPFD estimation models applied to the Puechabon testing dataset. Additionally, Table 4.1 presents the statistical result of total PPFD estimation in Puechabon utilizing these models. A review of the statistical results in Table 4.1 and the estimation errors in Figure B.5 suggests that Model 2 is the most accurate among the three models and the performance of Model 3 is comparable to that of Model 2. Model 1 consistently tends to underestimate the PPFD values in relation to actual measurements, a tendency also observed, though to a lesser extent, in Model 3.

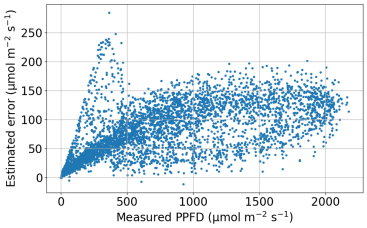

(a) Scatter plot depicting the estimation errors versus the measured PPFD values for Model 1.

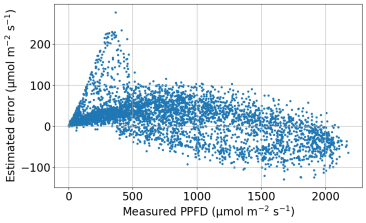

(b) Scatter plot depicting the estimation errors versus the measured PPFD values for Model 2.

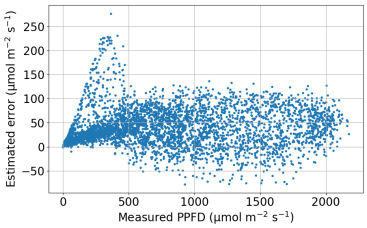

(c) Scatter plot depicting the estimation errors versus the measured PPFD values for Model 3.

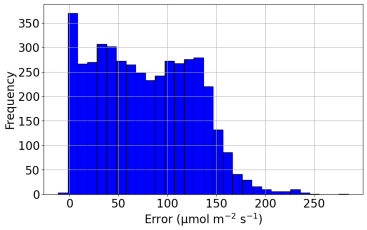

(d) Histogram of the estimation errors for Model 1.

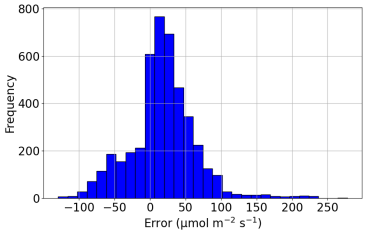

(e) Histogram of the estimation errors for Model 2.

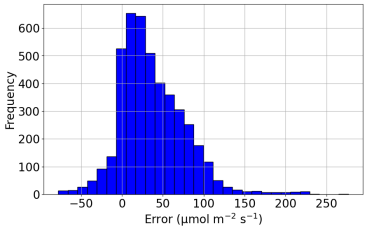

(f) Histogram of the estimation errors for Model 3.

Figure B.5: Histograms and scatterplots illustrating the estimated errors of the three distinct models for Puechabon (FR)

B.1.6 Lamasquere (FR)

Figure B.6 illustrates scatter plots and histograms of the estimation errors for three PPFD estimation models applied to the Lamasquere testing dataset. Furthermore, Table 4.1 presents the statistical result of total PPFD estimation in Lamasquere using these three models. An examination of the statistical results in Table 4.1 and the and the error patterns shown in Figure B.6 suggests Models 2 and 3 are the best performing models and show similar overall performance. However, Model 2 displays a slight advantage in performance over Model 3.

B.1.7 Castelporziano2 (IT)

Figure B.7 shows scatter plots and histograms of the estimation errors for three PPFD estimation models applied to the Castelporziano2 testing dataset. Addition-

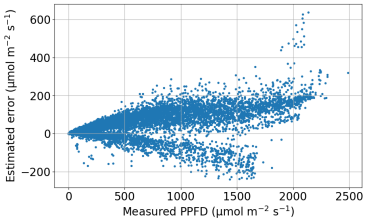

(a) Scatter plot depicting the estimation errors versus the measured PPFD values for Model 1.

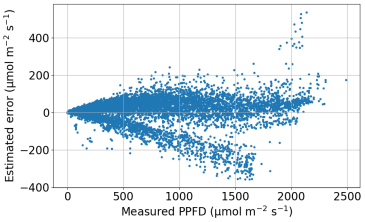

(b) Scatter plot depicting the estimation errors versus the measured PPFD values for Model 2.

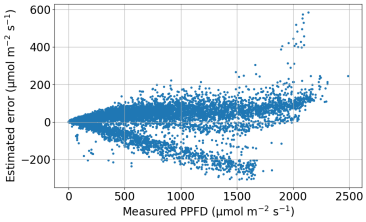

(c) Scatter plot depicting the estimation errors versus the measured PPFD values for Model 3.

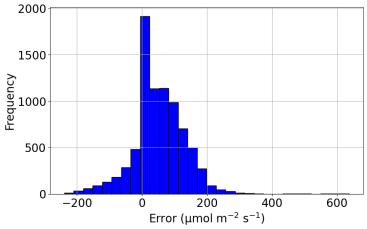

(d) Histogram of the estimation errors for Model 1.

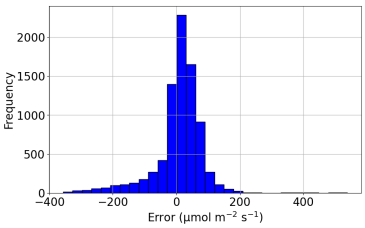

(e) Histogram of the estimation errors for Model 2.

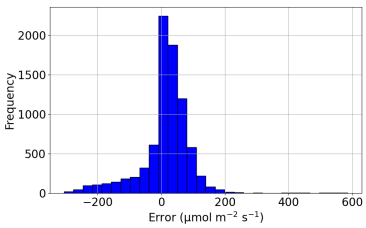

(f) Histogram of the estimation errors for Model 3.

Figure B.6: Histograms and scatterplots illustrating the estimated errors of the three distinct models for Lamasquere (FR)

ally, Table 4.1 presents the statistical result of total PPFD estimation in Castelporziano2 utilizing these models. A review of the statistical results in Table 4.1 and the visual results shown in Figure B.7 indicates that Model 2 is the most effective model among the three. The result also suggest that Models 1 and 3 almost consistently tend to underestimate PPFD values compared to the actual measurements. However, Model 3 displays better performance compared to Model 1.

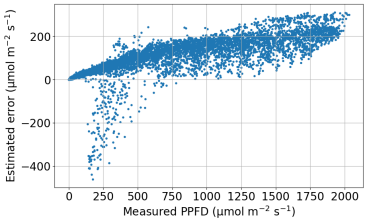

(a) Scatter plot depicting the estimation errors versus the measured PPFD values for Model 1.

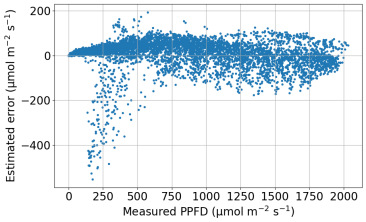

(b) Scatter plot depicting the estimation errors versus the measured PPFD values for Model 2.

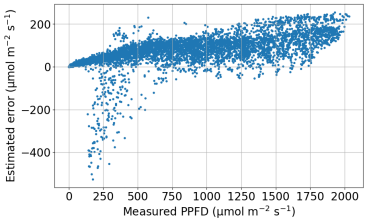

(c) Scatter plot depicting the estimation errors versus the measured PPFD values for Model 3.

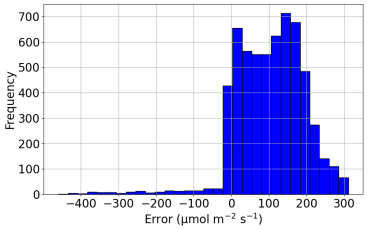

(d) Histogram of the estimation errors for Model 1.

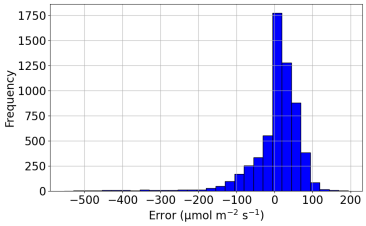

(e) Histogram of the estimation errors for Model 2.

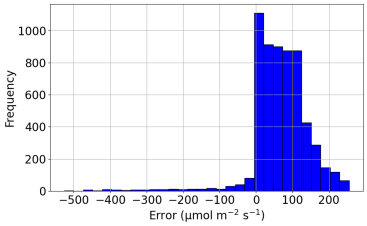

(f) Histogram of the estimation errors for Model 3.

Figure B.7: Histograms and scatterplots illustrating the estimated errors of the three distinct models for Castelporziano2 (IT)

B.2 Result for estimating diffuse PPFD in three location in Europe

B.2.1 Voulundgaard (DK)

Figure B.8 shows scatter plots and histograms of the estimation errors for three diffuse PPFD estimation models applied to the Voulundgaard test dataset. Additionally, Table 4.2 presents the statistical result of diffuse PPFD estimation in Voulundgaard utilizing these models. A review of the statistical results in Table 4.2 and the visual results shown in Figure B.8 indicates that Models A and C both tend to overestimate diffuse PPFD values compared to the actual measurements particularly for values associated with higher diffuse PPFD measurements. However, Model A demonstrates a better performance compared to Model C. Amongst the three models, Model B shows the best performance.

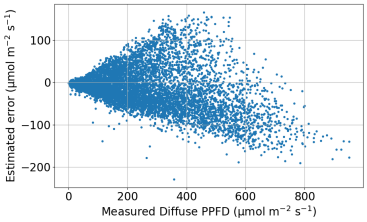

(a) Scatter plot illustrating the estimation errors versus the measured diffuse PPFD values for Model A.

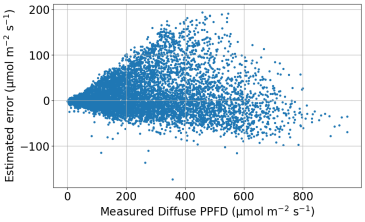

(b) Scatter plot illustrating the estimation errors versus the measured diffuse PPFD values for Model B.

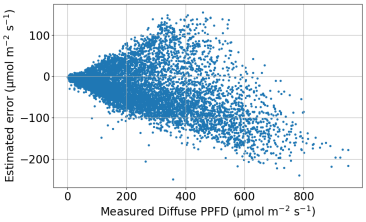

(c) Scatter plot illustrating the estimation errors versus the measured diffuse PPFD values for Model C.

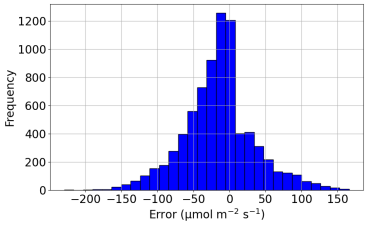

(d) Histogram of the estimation errors for Model A.

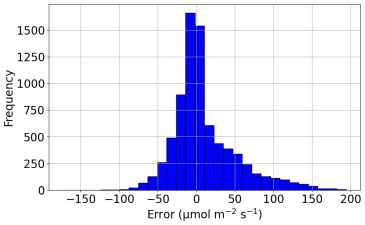

(e) Histogram of the estimation errors for Model B.

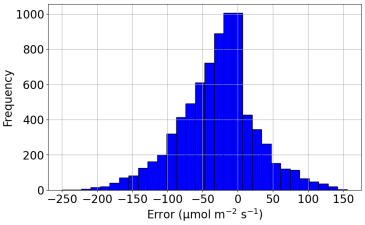

(f) Histogram of the estimation errors for Model C.

Figure B.8: Histograms and scatterplots illustrating the estimation errors of the three distinct models for estimating diffuse PPFD for Voulundgaard (DK)

B.2.2 Gebesee (DE)

Figure B.9 displays scatter plots and histograms of the estimation errors for three unique PPFD estimation models applied to the Gebesee testing dataset. Additionally, Table 4.2 presents the statistical result of diffuse PPFD estimation in Gebesee using these models. A review of the statistical results in Table 4.2 and the estimation errors in Figure B.9 suggests that the overall performance of the three models is quite similar. All the models appear mostly to underestimate diffuse PPFD values when compared to actual measurements, with Models B and C showing a marginally better performance than Model A.

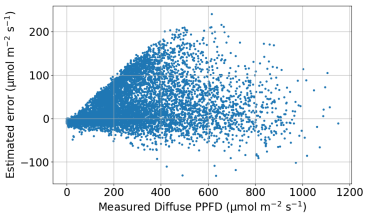

(a) Scatter plot illustrating the estimation errors versus the measured diffuse PPFD values for Model A.

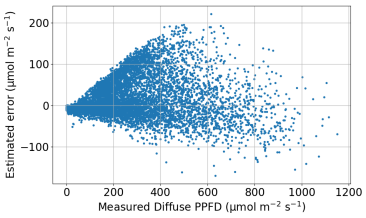

(b) Scatter plot illustrating the estimation errors versus the measured diffuse PPFD values for Model B.

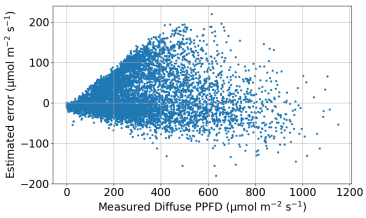

(c) Scatter plot illustrating the estimation errors versus the measured diffuse PPFD values for Model C.

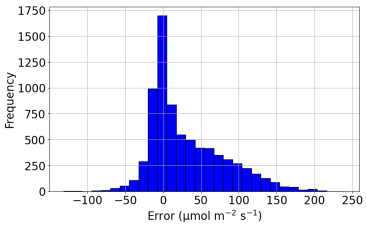

(d) Histogram of the estimation errors for Model A.

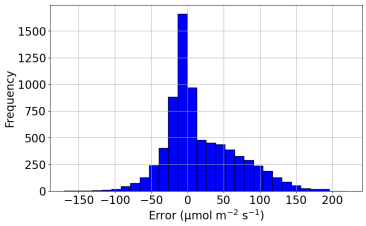

(e) Histogram of the estimation errors for Model B.

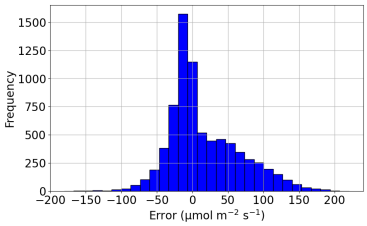

(f) Histogram of the estimation errors for Model C.

Figure B.9: Histograms and scatterplots illustrating the estimation errors of the three distinct models for estimating diffuse PPFD for Gebesee (DE)

B.2.3 Lamasquere (FR)

Figure B.10 shows scatter plots and histograms illustrating the estimation errors of three distinct diffuse PPFD estimation models when applied to the Lamasquere test dataset. Furthermore, Table 4.2 details the statistical result of diffuse PPFD estimation in Lamasquere using these three methods. A review of both the statistical result in Table 4.2 and the estimation errors in Figure B.10 indicates that the overall performance of all the models is very similar. Model B, showing a slightly better outcome compared to Models C, is the best performing model among the three.

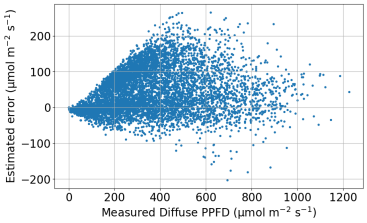

(a) Scatter plot illustrating the estimation errors versus the measured diffuse PPFD values for Model A.

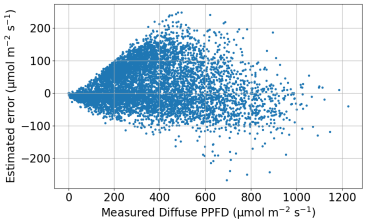

(b) Scatter plot illustrating the estimation errors versus the measured diffuse PPFD values for Model B.

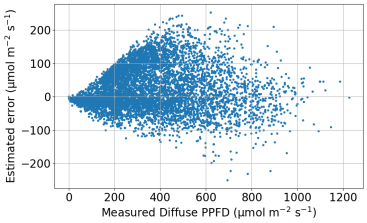

(c) Scatter plot illustrating the estimation errors versus the measured diffuse PPFD values for Model C.

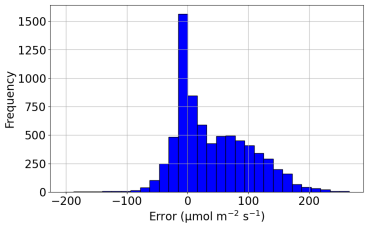

(d) Histogram of the estimation errors for Model A.

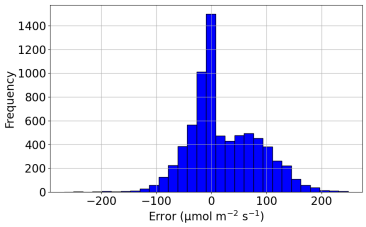

(e) Histogram of the estimation errors for Model B.

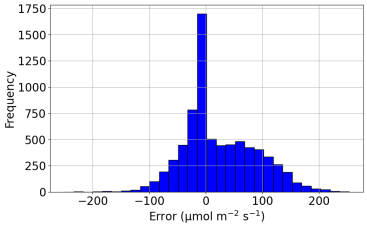

(f) Histogram of the estimation errors for Model C.

Figure B.10: Histograms and scatterplots illustrating the estimation errors of the three distinct models for estimating diffuse PPFD for Lamasquere (FR)

Bibliography

[1] M. S. Ahmed and M. R. Khan. "Assessing Agrivoltaics: Crops Under Solar Panels, or Solar Panels Over Crops?" In: *2023 IEEE Region 10 Symposium (TENSYMP)*. Canberra, Australia, 2023, pp. 1–4. DOI: 10.1109/TENSYMP55890.2023.10223638.

[2] M. Sojib Ahmed et al. "Agrivoltaics analysis in a techno-economic framework: Understanding why agrivoltaics on rice will always be profitable". In: *Appl. Energy* 323 (Oct. 2022), p. 119560.

[3] S. Amaducci, X. Yin, and M. Colauzzi. "Agrivoltaic systems to optimise land use for electric energy production". In: *Appl Energy* 220 (2018), pp. 545–61. DOI: https://doi.org/10.1016/j.apenergy.2018.03.081.

[4] K. Anderson and M. Mikofski. *Slope-Aware Backtracking for Single-Axis Trackers*. Technical Report NREL/TP-5K00-76626. NREL, 2020. URL: https://www.nrel.gov/docs/fy20osti/76626.pdf.

[5] E. B. Babatunde, ed. *Solar Radiation*. InTech, 2012. DOI: 10.5772/1949.

[6] Christian Brümmer, Jean-Pierre Delorme, and Frederik Schrader. *ETC L2 Meteo, Gebesee, 2019-12-31–2023-10-31*. https://hdl.handle.net/11676/9R2D2w2cjWizN4ffDBGDIG8g. Copyright: http://meta.icos-cp.eu/ontologies/cpmeta/icosLicence. 2023. DOI: 11676/9R2D2w2cjWizN4ffDBGDIG8g.

[7] Aurore Brut et al. *ETC L2 Meteo, Lamasquere, 2019-12-31–2023-09-30*. https://hdl.handle.net/11676/GCkvtADnF7irstUyzpTvbmY7. Copyright: http://meta.icos-cp.eu/ontologies/cpmeta/icosLicence. 2023. DOI: 11676/GCkvtADnF7irstUyzpTvbmY7.

[8] P.E. Campana et al. "Optimisation of vertically mounted agrivoltaic systems". In: *J Clean Prod* 325 (2021), p. 129091. DOI: https://doi.org/10.1016/j.jclepro.2021.129091.

[9] Y. Cascone, V. Corrado, and V. Serra. "Calculation procedure of the shading factor under complex boundary conditions". In: *Sol Energy* 85 (2011), pp. 2524–2539. DOI: https://doi.org/10.1016/j.solener.2011.07.011.

[10] H. Dinesh and J.M. Pearce. "The potential of agrivoltaic systems". In: *Renew Sustain Energy Rev* 54 (2016), pp. 299–308.

[11] D. G. Dye. "Spectral composition and quanta-to-energy ratio of diffuse photosynthetically active radiation under diverse cloud conditions". In: *J. Geophys. Res.* 109 (2004), p. D10203. DOI: 10.1029/2003JD004251.

[12] Silvano Fares et al. *ETC L2 Meteo, Castelporziano2, 2020-12-31–2023-10-31*. https://hdl.handle.net/11676/b9jFmI9WtonRGMRRsWOeBQK9. Copyright: http://meta.icos-cp.eu/ontologies/cpmeta/icosLicence. 2023. DOI: 11676/b9jFmI9WtonRGMRRsWOeBQK9.

[13] I Foyo-Moreno, I Alados, and L Alados-Arboledas. "A new empirical model to estimate hourly diffuse photosynthetic photon flux density". In: *Atmospheric Research* 203 (2018), pp. 189–196. DOI: 10.1016/j.atmosres.2017.12.012. URL: https://doi.org/10.1016/j.atmosres.2017.12.012.

[14] I. Foyo-Moreno, I. Alados, and L. Alados-Arboledas. "Title of the Article". In: *International Journal of Climatology* 37.Suppl.1 (2017), pp. 1067–1075. DOI: 10.1002/joc.5063. URL: https://doi.org/10.1002/joc.5063.

[15] Thomas Friborg, Rasmus Jensen, and Lars Rasmussen. *ETC L2 Meteo, Voulundgaard, 2019-12-31–2023-08-31*. https://hdl.handle.net/11676/Re3qInPTNvjNGwYd8opFrpHc. Copyright: http://meta.icos-cp.eu/ontologies/cpmeta/icosLicence. 2023. DOI: 11676/Re3qInPTNvjNGwYd8opFrpHc.

[16] A. Goetzberger and A. Zastrow. "On the Coexistence of Solar-Energy Conversion and Plant Cultivation". In: *International Journal of Solar Energy* 1 (1982), pp. 55–69. DOI: 10.1080/01425918208909875.

[17] Michal Heliasz et al. *ETC L2 Meteo, Hyltemossa, 2017-12-31–2023-08-31*. https://hdl.handle.net/11676/25C6MtXdS6TBGxKKc4HbMfGA. Copyright: http://meta.icos-cp.eu/ontologies/cpmeta/icosLicence. 2023. DOI: 11676/25C6MtXdS6TBGxKKc4HbMfGA.

[18] William F Holmgren, Clifford W Hansen, and Mark A Mikofski. "pvlib python: a python package for modeling solar energy systems". In: *Journal of Open Source Software* 3.29 (2018), p. 884. DOI: 10.21105/joss.00884. URL: https://doi.org/10.21105/joss.00884.

[19] Bo Hu, Yuesi Wang, and Guangren Liu. "Spatiotemporal characteristics of photosynthetically active radiation in China". In: *Journal of Geophysical Research* 112 (July 2007). DOI: 10.1029/2006JD007965.

[20] T. Huld, R. Müller, and A. Gambardella. "A new solar radiation database for estimating PV performance in Europe and Africa". In: *Solar Energy* 86 (2012), pp. 1803–1815. DOI: 10.1016/j.solener.2012.03.006.

[21] Thomas Huld et al. "Assembling Typical Meteorological Year Data Sets for Building Energy Performance Using Reanalysis and Satellite-Based Data". In: *Atmosphere* 9.2 (2018), p. 53. DOI: 10.3390/atmos9020053. URL: https://doi.org/10.3390/atmos9020053.

[22] Andreas Ibrom et al. *ETC L2 Meteo, Soroe, 2020-12-31–2023-10-31*. https://hdl.handle.net/11676/i3g5rtkRTRI7NoNrKgSHKlmv. Copyright: http://meta.icos-cp.eu/ontologies/cpmeta/icosLicence. 2023. DOI: 11676/i3g5rtkRTRI7NoNrKgSHKlmv.

[23] C.P. Jacovides et al. "The dependence of global and diffuse PAR radiation components on sky conditions at Athens, Greece". In: *Agricultural and Forest Meteorology* 143 (2007), pp. 277–287.

[24] Hamlyn G. Jones. *Plants and Microclimate: A Quantitative Approach to Environmental Plant Physiology*. 3rd ed. Cambridge University Press, 2013. DOI: 10.1017/CBO9780511845727. URL: https://doi.org/10.1017/CBO9780511845727.

[25] G. S. Kuaban et al. "Smart Sustainable Agrivoltaics Systems: The Future of Sustainable Agricultural Technology (Agri-tech) and Green Energy". In: *2023 3rd International Conference on Electrical, Computer, Communications and Mechatronics Engineering (ICECCME)*. Tenerife, Canary Islands, Spain, 2023, pp. 1–6. DOI: 10.1109/ICECCME57830.2023.10253215.

[26] D.H.W. Li and J.C. Lam. "Predicting solar irradiance on inclined surfaces using sky radiance data". In: *Energy Conversion and Management* 45 (2004), pp. 1771–1783.

[27] Jean-Marc Limousin, Jean Kempf, and Jean-Marc Ourcival. *ETC L2 Meteo, Puechabon, 2020-12-31–2023-10-31*. https://hdl.handle.net/11676/LuD-xh31A42o8jebIKm6TbIv. Copyright: http://meta.icos-cp.eu/ontologies/cpmeta/icosLicence. 2023. DOI: 11676/LuD-xh31A42o8jebIKm6TbIv.

[28] E. Lorenzo, L. Narvarte, and J. Muñoz. "Tracking and back-tracking". In: *Progress in Photovoltaics: Research and Applications* 19 (2011), pp. 747–753. DOI: https://doi.org/10.1002/pip.1085.

[29] H. Marrou, J. Wery, L. Dufour, et al. "Productivity and radiation use efficiency of lettuces grown in the partial shade of photovoltaic panels". In: *Eur J Agron* 44 (2013), pp. 54–66. DOI: https://doi.org/10.1016/j.eja.2012.08.003.

[30] Edward L. Maxwell. *A Quasi-Physical Model for Converting Hourly Global Horizontal to Direct Normal Insolation*. Tech. rep. SERI/TR-215-3087. Golden, CO: Solar Energy Research Institute, 1987.

[31] msm. *Rotation around non-zero point*. Mathematics Stack Exchange. Accessed on July 26, 2023, URL: https://math.stackexchange.com/q/1964921 (version: 2016-10-12). 2016. URL: https://math.stackexchange.com/q/1964921.

[32] A. Niewienda and F. Heidt. "SOMBRERO: A PC-tool to calculate shadows on arbitrarily oriented surfaces". In: *Sol Energy* 58.4 (1996). Selected proceedings of the ISES 1995: Solar World Congress. Part II, pp. 253–63. DOI: https://doi.org/10.1016/S0038-092X(96)00088-6.

[33] MMA Noriega-Gardea et al. "Modeling photosynthetically active radiation: a review". In: *Atmósfera* 34.3 (2021), pp. 357–370. DOI: 10.20937/ATM.52737. URL: https://doi.org/10.20937/ATM.52737.

[34] Matthias Peichl et al. *ETC L2 Meteo, Svartberget, 2018-12-31–2023-08-31*. https://hdl.handle.net/11676/u-hkdDrF_EEFXNTA_0QIgh5H. Copyright: http://meta.icos-cp.eu/ontologies/cpmeta/icosLicence. 2023. DOI: 11676/u-hkdDrF_EEFXNTA_0QIgh5H.

[35] *Photovoltaic Geographical Information System (PVGIS) - Getting Started with PVGIS*. https://joint-research-centre.ec.europa.eu/photovoltaic-geographical-information-system-pvgis/getting-started-pvgis/pvgis-user-manual_en. Accessed on 5th October 2023.

[36] *PVGIS Typical Meteorological Year (TMY) Generator*. Joint Research Centre, European Commission. Retrieved from https://joint-research-centre.ec.europa.eu/photovoltaic-geographical-information-system-pvgis/pvgis-tools/pvgis-typical-meteorological-year-tmy-generator_en. 2024.

[37] *PVsyst*. https://www.pvsyst.com/. Accessed: 2023-10-05.

[38] V. Quaschning and R. Hanitsch. "Irradiance calculation on shaded surfaces". In: *Sol Energy* 62 (1998), pp. 369–75. DOI: https://doi.org/10.1016/s0038-092x(98)00018-8.

[39] V. Quaschning and R. Hanitsch. "Shade calculations in photovoltaic systems". In: *Proceedings of the 1995 ISES Solar World Conference*. 1995, pp. 1–5.

[40] I. Reda and A. Andreas. "Solar position algorithm for solar radiation applications". In: *Solar Energy* 76.5 (2004), pp. 577–589.

[41] Matthew Reno, Clifford Hansen, and Joshua Stein. *Global Horizontal Irradiance Clear Sky Models: Implementation and Analysis*. Tech. rep. SAND2012-2389. Sandia National Laboratories, 2012.

[42] Marius Schmidt et al. *ETC L2 Meteo, Selhausen Juelich, 2018-12-31–2023-09-30*. https://hdl.handle.net/11676/cKK64KrRLa1_QzR5aPi89MmF. Copyright: http://meta.icos-cp.eu/ontologies/cpmeta/icosLicence. 2023. DOI: 11676/cKK64KrRLa1_QzR5aPi89MmF.

[43] T. Sekiyama and A. Nagashima. "Solar Sharing for Both Food and Clean Energy Production: Performance of Agrivoltaic Systems for Corn, A Typical Shade-Intolerant Crop". In: *Environments* 6 (2019), p. 65.

[44] J. W. Spencer. "Fourier series representation of the position of the sun". In: *Search* 2.5 (May 1971), pp. 172+. URL: http://www.mail-archive.com/sundial@uni-koeln.de/msg01050.html.

[45] R. W. Thimijan and R. D. Heins. "Photometric, Radiometric, and Quantum Light Units of Measure: A Review of Procedures for Interconversion". In: *Hortscience* 18.6 (1983), pp. 818–822.

[46] Lucien Wald. *Fundamentals of Solar Radiation*. 1st ed. CRC Press, 2021. DOI: 10.1201/9781003155454. URL: https://doi-org.ludwig.lub.lu.se/10.1201/9781003155454.

[47] A. Weselek et al. "Agrivoltaic system impacts on microclimate and yield of different crops within an organic crop rotation in a temperate climate". In: *Agronomy for Sustainable Development* 41 (2021), p. 59. DOI: https://doi.org/10.1007/s13593-021-00714-y.

[48] A. Weselek et al. "Effects on Crop Development, Yields and Chemical Composition of Celeriac (Apium graveolens L. var. rapaceum) Cultivated Underneath an Agrivoltaic System". In: *Agronomy* 11.4 (2021), p. 733. DOI: https://doi.org/10.3390/agronomy11040733.

[49] A. Yezioro and E. Shaviv. "A design tool for analyzing mutual shading between buildings". In: *Solar Energy* 52 (1994), pp. 27–37.

[50] S. Zainali et al. “Direct and diffuse shading factors modelling for the most representative agrivoltaic system layouts”. In: *Appl Energy* 339 (2022), p. 120981. DOI: https://doi.org/10.1016/j.apenergy.2023.120981.

Master's Theses in Mathematical Sciences 2024:E14
ISSN 1404-6342

LUNFMS-3125-2024

Mathematical Statistics
Centre for Mathematical Sciences
Lund University
Box 118, SE-221 00 Lund, Sweden

http://www.maths.lu.se/